

Semiclassical analysis of polarization effects in collision-induced intramultiplet mixing for $\text{Ne}^{**}\{(2p)^5(3p)\} + \text{He}$

M. P. I. Manders, W. B. M. van Hoek, E. J. D. Vredenburg, G. J. Sandker,
H. C. W. Beijerinck, and B. J. Verhaar

Physics Department, Eindhoven University of Technology, P.O. Box 513, 5600 MB Eindhoven, The Netherlands

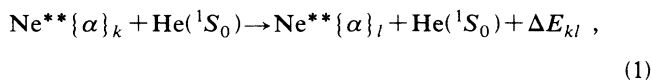
(Received 31 May 1988)

We have performed new crossed-beam measurements and quantum-mechanical calculations on transitions between the short-lived $\text{Ne}^{**}\{(2p)^5(3p)\}_k \equiv \{\alpha\}_k$ states with $k=4,5,6,7$ (Paschen numbering), induced by collisions with ground-state He atoms at energies between 70 and 140 meV. The $\{\alpha\}_{4,5,6,7}$ multiplet is distinguished by the presence of several avoided crossings between the adiabatic potentials $V_k^{\text{el}}(R)$ —a sign of strong, localized radial coupling. This has inspired a simple, semiclassical model for the Ne^{**} -He collision process, which has the following ingredients: (i) straight-line trajectories with hard-sphere scattering at the classical turning point R_T ; (ii) rotational coupling for $R > R_L$ and “locking” of the electronic angular momentum \mathbf{J} to the internuclear axis for $R \leq R_L$, with R_L the locking radius; (iii) Landau-Zener-type curve-crossing transitions near the crossing radius R_C . This model goes a long way toward explaining the experimental polarization effects, i.e., differences between polarized cross sections $Q_{l \leftarrow k}^{M_k}$ for the $\{\alpha\}_k \rightarrow \{\alpha\}_l$ transition depending on the asymptotic orientation of the total electronic angular momentum \mathbf{J} , as specified by the magnetic quantum number M_k . These polarization effects are at times very large. For example, at a center-of-mass collision energy $E \simeq 100$ meV, we find $Q_{l \leftarrow 5}^{01}/Q_{l \leftarrow 5}^{11} = 0.52$ and 3.5 for $l=6$ and 7, respectively, $Q_{l \leftarrow 6}^{01}/Q_{l \leftarrow 6}^{11} = 0.41$ and 1.3 for $l=5$ and 7, and $Q_{l \leftarrow 7}^{01}/Q_{l \leftarrow 7}^{11} = 0.08$ and 8.9 for $l=4$ and 5.

I. INTRODUCTION

In recent years there has been a rise in the attention paid to inelastic collisions of atoms in short-lived electronically excited states.¹⁻¹⁷ A recent review of the field was given by Hertel *et al.*,¹⁸ while the basics of our own work were set out in earlier papers.¹⁹⁻²¹ Excitation by a polarized laser prepares the short-lived states in well-defined asymptotic orientations. Strong effects of the orientation on cross-section magnitude have been observed. In many cases, however, a satisfactory explanation of these polarization effects proves elusive, due to lack of accurate information on coupling potentials for the systems under consideration.

A fundamentally different situation obtains with the inelastic intramultiplet-mixing process



where $\{\alpha\}_j = \{(2p)^5(3p)\}_j$, with j running from 1 to 10 with decreasing energy. Here, all three ingredients necessary for a better understanding are available: experimental data, potential surface information, and the capability to perform fully quantum-mechanical coupled-channel calculations.

First, we have obtained experimental results on polarized-atom inelastic cross sections from a crossed-beam experiment, for a well-defined translational energy and asymptotic orientation of the initial state $\{\alpha\}_k$.²⁰ Careful design of the crossed-beam apparatus,²¹ necessi-

tated by the short lifetimes of the Ne^{**} states ($\tau \simeq 20$ ns) and the small transition cross sections ($Q_{l \leftarrow k} \simeq 1 \text{ \AA}^2$), has resulted in large signals (1 kHz/ \AA^2) for the fluorescence from the final state $\{\alpha\}_l$ and a relatively low background (2–15 kHz). Absolute polarized-atom cross sections $Q_{l \leftarrow k}^{M_k}$ were presented earlier²⁰ for the $\{\alpha\}_5 \rightarrow \{\alpha\}_4$, $\{\alpha\}_6$, $\{\alpha\}_7$, and $\{\alpha\}_6 \rightarrow \{\alpha\}_7$ transitions. Here M_k is the magnetic quantum number of the intrinsic electronic angular momentum \mathbf{J} along the asymptotic relative velocity \mathbf{g} , i.e., the z axis. We observe large polarization effects. Typical results at center-of-mass energy $E \simeq 100$ meV are $Q_{l \leftarrow 5}^{01}/Q_{l \leftarrow 5}^{11} = 1.06$, 0.52, and 3.5 for $l=4$, 6, and 7, respectively.

Secondly, we have at our disposal Ne^{**} -He model potentials.^{1,11} They have been calculated starting from a three-particle model, in which the system is taken to consist of the $\text{Ne}^+(2p)^5$ core, the $e^-(3p)$ valence electron, and the $\text{He}(^1S_0)$ target. Thus are obtained, for internuclear distances $R \gtrsim 4.5a_0$, separate basic potentials $V_{\sigma}^{\text{el}}(R)$ and $V_{\pi}^{\text{el}}(R)$ for the $\sigma \equiv (|m_l|_{z'}=0)$ and $\pi \equiv (|m_l|_{z'}=1)$ orientations of the $3p$ orbital of the valence electron with respect to the internuclear axis, i.e., the z' axis. Tentatively extended by us down to $R \gtrsim 2.0a_0$,²⁰ and supplemented²⁰ by potentials $V_{\sigma}^{\text{core}}(R)$ and $V_{\pi}^{\text{core}}(R)$ for the two orientations of the core hole, derived from the spectroscopy of the $(\text{NeHe})^+$ ion,^{22,23} these allow calculation of the matrix elements of the Ne^{**} -He electronic Hamiltonian H_{el} in the atomic $|LSJM_J\rangle$ basis.^{1,11} Here L , S , and J are the quantum numbers of the electronic orbital, spin, and total angular momenta \mathbf{L} , \mathbf{S} , and \mathbf{J} , respectively. Diagonalization of

H_{el} then yields the adiabatic eigenstates $|\alpha_k J_k \Omega_k(R)\rangle$ and potential curves $V_k^\Omega(R)$, where $\Omega_k \equiv |M_k|_{z'}$. The 23 adiabatic potentials are divided into Ω manifolds. For $\Omega=0$, the further restraint of reflection symmetry of the molecular states generates distinct $+$ and $-$ classes, each containing five states with even and odd J , respectively.

A third instrument for a better understanding is our fully quantum-mechanical coupled-channel calculation, using the above potential as input.²⁰ These are performed in a basis of diabatic functions $|\pi\alpha J \Omega P M_P\rangle$ which, besides being atomic eigenfunctions $|\alpha J \Omega\rangle$, have definite parity π and well-defined quantum numbers P , $M_{P,z}$, and $\Omega = |M_J|_{z'} = |M_P|_{z'}$ for the P^2 , P_z , and $P_z = J_{z'}$ operators of the total angular momentum \mathbf{P} . The time-independent Schrödinger equation for the $\text{Ne}^{**}\text{-He}$ scattering problem then gives rise to a set of at most 18 coupled differential equations for each value of P and parity $\pi = \pm 1$. In this “ Ω -diabatic” representation, we have “physical” coupling by the molecular interaction $V_{\text{mol}} = V^{\text{Ne}^{**}\text{-He}}$ and rotational coupling by the operator T_{rot} of rotational nuclear motion. Our coupled-channel code uses a modified Numerov integration method.²⁴ We limit the calculation to impact parameters $b \lesssim 15a_0$, beyond which the nondiagonal matrix elements of $V^{\text{Ne}^{**}\text{-He}}$ vanish. For a $\text{Ne}^{**}\text{-He}$ collision energy $E = 100$ meV this implies $P \lesssim 100$. A complete calculation with appropriate integration step size $\Delta R = 0.02a_0$ then requires about 2.5 h on a Burroughs B7900 main-frame computer and yields cross sections that generally agree well with experiment.²⁰

Unfortunately, by their very nature, the quantum-mechanical calculations constitute essentially a “black box.” The link between input (model potentials) and output (cross sections) is rather remote. At this point, an analysis in semiclassical terms, if at all feasible, becomes highly desirable.

Our experiment, in its present form, involves $\text{Ne}^{**} + \text{He}$ collisions at thermal energies $70 \lesssim E$ (meV) $\lesssim 200$. At these low energies, relative velocities of the colliding atoms are small compared to electron velocities. This implies a quasimolecular system. Just as the molecular adiabatic electronic eigenfunctions $|\alpha_k J_k \Omega_k(R)\rangle$ are likely to offer a fair description of the electronic states, so are the adiabatic potentials $V_k^\Omega(R)$ apt to govern the relative motion of the nuclei. A completely adiabatic picture of the collision process of course precludes the possibility of transitions between different states. In general, the molecular electronic states will still be coupled by nuclear motion. The coupling between adiabatic states is bound to be particularly strong at so-called avoided crossings of the adiabatic potentials. It has long been established²⁵ that the nonadiabatic (radial) coupling at an avoided crossing lends itself particularly well to a semiclassical description. As we shall see, not only do several avoided crossings occur between the $\text{Ne}^{**}\text{-He}$ adiabatic potentials, but in addition they are limited to the quasiclosed multiplet of $\{\alpha\}_{4,5,6,7}$ states. Under the circumstances, semiclassical theory would appear to provide a natural framework for the discussion of a number of important $\{\alpha\}_k \rightarrow \{\alpha\}_l$ transitions.

In the present paper our aim is to obtain more insight into the physics involved in the collision than is provided by black-box-type quantum-mechanical calculations. As to absolute values of inelastic cross sections, the semiclassical approach is somewhat of a standard procedure. However, as an essential extension, we include the prediction of polarization effects by way of a physically suitable description of rotational coupling.

In Sec. II we present new experimental results for the $\{\alpha\}_{4,5,6,7}$ group of states, which allow a better test of our semiclassical model. In Sec. III the basic concepts of semiclassical theory, i.e., the Landau-Zener approach to radial coupling at an avoided crossing and the weighing of rotational coupling against “locking,” are discussed and related to the $\text{Ne}^{**}\text{-He}$ system. This is followed, in Sec. IV, by the description of a semiclassical model for calculating polarized-atom inelastic cross sections, which permits, in combination with experimental results and quantum-mechanical calculations, a “complete” analysis for this system. Finally, in Sec. V, we offer some concluding remarks.

II. NEW EXPERIMENTAL RESULTS

We present new $\text{Ne}^{**}\text{-He}$ measurements on polarization effects, complementing those reported earlier for the $\{\alpha\}_5 \rightarrow \{\alpha\}_{4,6,7}$ and $\{\alpha\}_6 \rightarrow \{\alpha\}_7$ transitions.²⁰ Figures 1–3 and 4–6 show observed cross sections for the $\{\alpha\}_6 \rightarrow \{\alpha\}_{4,5,7}$ and $\{\alpha\}_7 \rightarrow \{\alpha\}_{4,5,6}$ transitions, as a function of the angle β between the laser electric field vector \mathbf{E} and the asymptotic relative velocity \mathbf{g} of the collision

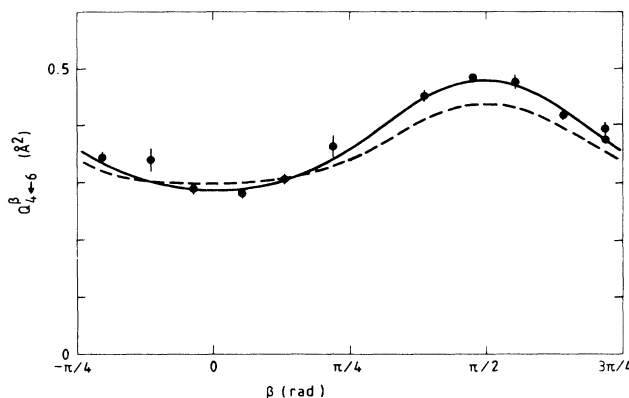


FIG. 1. Experimental results for the observed cross section Q_{4-6}^β , as a function of the angle β between the electric field \mathbf{E} of the laser and the average relative velocity \mathbf{g} , at a center-of-mass energy $E_6 \approx 100$ meV. Statistical errors only have been indicated. The solid line (—) represents a curve fit of the data points according to Eqs. (2) and (5), assuming the absence of a magnetic field. The dashed line (---) is the result of quantum-mechanical calculations with the extended model potentials of Hennecart and Masnou-Seeuws as input. It uses a weighted average of quantum-mechanical cross sections $Q_{4-7}^{M_J}$, assuming Gaussian primary- and secondary-beam velocity distributions.

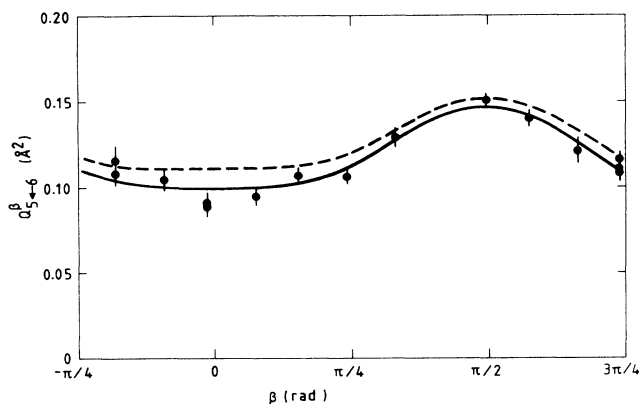


FIG. 2. Experimental results for the observed cross section Q_{5-6}^β at $E_6 \approx 100$ meV. See caption of Fig. 1 for further detail.

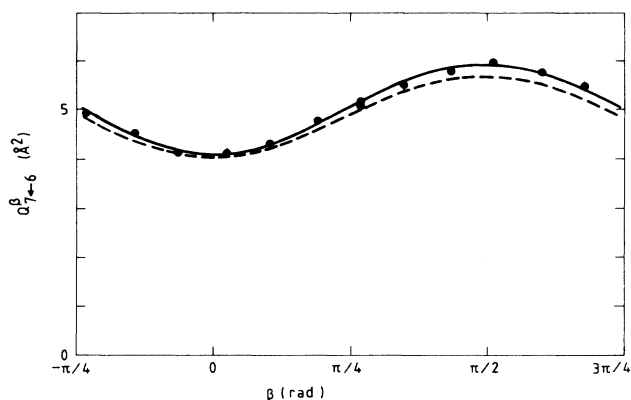


FIG. 3. Experimental results for the observed cross section Q_{7-6}^β at $E_6 \approx 110$ meV. See caption of Fig. 1 for further detail.

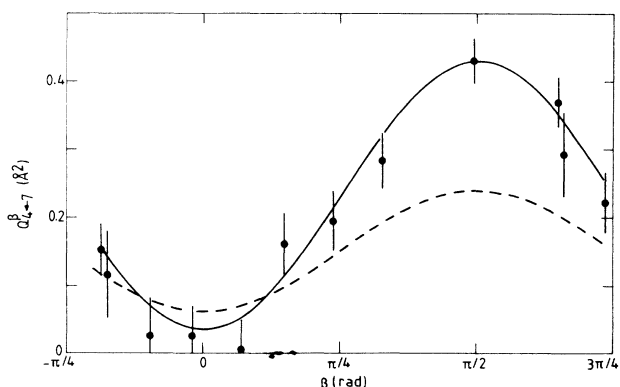


FIG. 4. Experimental results for the observed cross section Q_{4-7}^β at $E_7 \approx 95$ meV. The curve fit of the data points (—) is according to Eqs. (2) and (4). This is a highly endothermic transition, with the threshold energy $\Delta E_{47} = 91$ meV close to the average experimental center-of-mass energy. See caption of Fig. 1 for further detail.

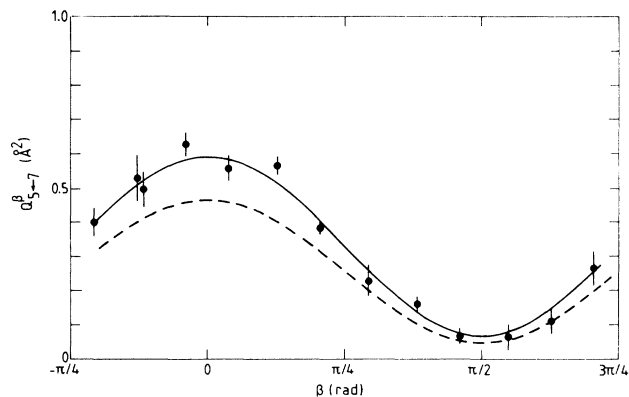


FIG. 5. Experimental results for the observed cross section Q_{5-7}^β at $E_7 \approx 95$ meV. The threshold energy is $\Delta E_{57} = 81$ meV. See caption of Fig. 2 for further detail.

partners. Center-of-mass energy is approximately $E = 100$ meV for these measurements. The absolute cross-section values are estimated to exhibit a systematic error of at most 30%. Table I gives the corresponding single- M_k -state polarized cross sections $Q_{l \leftarrow k}^{|M_k|}$. These have been determined from a least-squares fit of the data to a model function of the general form

$$Q_{l \leftarrow k}^\beta = \sum_{n=0}^{J_k} C_n^{J_k} \cos(2n\beta). \quad (2)$$

In detail,²¹

$$Q_{l \leftarrow k}^\beta = \sum_{m_k = -J_k}^{J_k} g_{m_k} \sum_{M_k = -J_k}^{J_k} \{d_{m_k M_k}^{J_k}(\beta)\}^2 Q_{l \leftarrow k}^{|M_k|}, \quad (3)$$

where the rotation matrices or reduced Wigner D functions d (Ref. 26) transform the initial distribution g_{m_k}

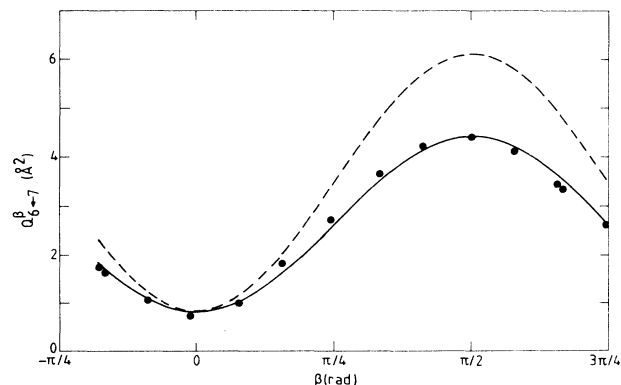


FIG. 6. Experimental results for the observed cross section Q_{6-7}^β at $E_7 \approx 95$ meV. The threshold energy being only $\Delta E_{67} = 24$ meV, averaging over different velocities has only a limited effect. See caption of Fig. 4 for further detail.

TABLE I. Experimental and quantum-mechanical polarized cross sections $Q_{l \leftarrow k}^{iM_k}$, at various center-of-mass energies E of the initial state $\{\alpha\}_k$, together with the polarization effect $Q_{l \leftarrow k}^{0i}/Q_{l \leftarrow k}^{1i}$. The extended potentials, used in the calculations, are identical to those used in Ref. 20. Where indicated, the experimental energy distribution has been taken into account in calculating effective quantum-mechanical cross sections.

Initial state $\{\alpha\}_k$	Final state $\{\alpha\}_l$	E_{cm} (meV)		$Q_{l \leftarrow k}^{0i}$ (\AA^2)		Cross section $Q_{l \leftarrow k}^{1i}$ (\AA^2)		$Q_{l \leftarrow k}^{2i}$ (\AA^2)		Polarization effect $Q_{l \leftarrow k}^{0i}/Q_{l \leftarrow k}^{1i}$	
		QM	Expt.	QM	Expt.	QM	Expt.	QM	Expt.	QM	Expt.
$\{\alpha\}_5$	$\{\alpha\}_4$	60	60	8.9	9.6	10.1	8.7			0.9	1.1
		100	100	14.4	13.2	13.7	12.5			1.0	1.1
		140	140	16.9	14.6	16.1	13.3			1.1	1.1
	$\{\alpha\}_6$	60	70	0.32	0.32	0.34	0.62			0.92	0.52
		100	100	0.66	0.50	0.93	0.97			0.71	0.52
		140	140	0.77	0.75	1.61	1.27			0.48	0.60
	$\{\alpha\}_7$	60	55	5.0	5.0	1.17	1.4			4.3	3.6
		100	100	7.1	7.0	1.91	2.0			3.7	3.5
		140	140	7.7	9.2	2.15	2.7			3.6	3.4
$\{\alpha\}_6$	$\{\alpha\}_4$	100 ^a	100	0.21	0.27	0.38	0.42	0.08	0.05	0.55	0.64
	$\{\alpha\}_5$	100 ^a	100	0.05	0.06	0.14	0.14	0.03	0.02	0.35	0.41
	$\{\alpha\}_7$	110 ^a	110	7.8	8.3	6.0	6.3	3.1	3.1	1.3	1.3
$\{\alpha\}_7$	$\{\alpha\}_4$	95 ^a	95	0.06	0.04	0.24	0.43			0.27	0.08
		140	140	0.43	0.44	1.3	1.3			0.33	0.33
	$\{\alpha\}_5$	95 ^a	95	0.46	0.59	0.05	0.07			9.3	8.9
		140	140	2.4	2.6	0.30	0.37			9.0	7.0
	$\{\alpha\}_6$	95 ^a	95	0.84	0.81	6.1	4.4			0.14	0.18
		140	140	2.1	2.0	9.7	7.2			0.22	0.28

^aExperimental velocity distribution taken into account.

over magnetic substates $|\alpha_k J_k m_k\rangle_E$ to a distribution over substates $|\alpha_k J_k M_k\rangle_g$. Upon excitation with a linearly polarized laser from the $|^3P_0, J_i=0\rangle$ metastable state, we have for an $|\alpha_k J_k=1\rangle$ initial state: $g_{|m_k|=0}=1$, $g_{|m_k|\neq 0}=0$. The coefficients in Eq. (2) are

$$C_0^1 = \frac{1}{2}(Q_{l \leftarrow k}^{0i} + Q_{l \leftarrow k}^{1i}), \quad (4)$$

$$C_1^1 = \frac{1}{2}(Q_{l \leftarrow k}^{0i} - Q_{l \leftarrow k}^{1i}).$$

For $|\alpha_k J_k=2\rangle$ and $|^3P_2, J_i=2\rangle$, again using a linearly polarized laser so that $g_{+m_k}=g_{-m_k}=g_{|m_k|}$, we can write

$$\begin{aligned} C_0^2 &= \frac{1}{64}[(22g_0 + 24g_1 + 18g_2)Q_{l \leftarrow k}^{0i} + (24g_0 + 64g_1 + 40g_2)Q_{l \leftarrow k}^{1i} + (18g_0 + 40g_1 + 70g_2)Q_{l \leftarrow k}^{2i}], \\ C_1^2 &= \frac{1}{64}[(24g_0 - 24g_2)Q_{l \leftarrow k}^{0i} + (32g_1 - 32g_2)Q_{l \leftarrow k}^{1i} + (-24g_0 - 32g_1 + 56g_2)Q_{l \leftarrow k}^{2i}], \\ C_2^2 &= \frac{1}{64}[(18g_0 - 24g_1 + 6g_2)Q_{l \leftarrow k}^{0i} + (-24g_0 + 32g_1 - 8g_2)Q_{l \leftarrow k}^{1i} + (6g_0 - 8g_1 + 2g_2)Q_{l \leftarrow k}^{2i}]. \end{aligned} \quad (5)$$

In the present case, as earlier for the $(\{\alpha\}_6, J_6=2)$ initial state,²⁰ the time-integrated distribution g_{m_k} over magnetic substates $|\alpha_k J_k m_k\rangle_E$ in the scattering volume was calculated assuming the absence of a magnetic field, with the result $g_{|m_k|=0}=0$, $g_{|m_k|=1} \approx \frac{1}{6}$, $g_{|m_k|=2} \approx \frac{2}{6}$. This leaves some room for error in the $\{\alpha\}_6 \rightarrow \{\alpha\}_l$ polarized cross sections.

The measurements disclose large variations, both in cross-section magnitude ($Q_{5 \leftarrow 7}^\beta \ll Q_{6 \leftarrow 7}^\beta$) and in polarization effects ($Q_{5 \leftarrow 7}^{0i}/Q_{5 \leftarrow 7}^{1i} \approx 8$, $Q_{6 \leftarrow 7}^{0i}/Q_{6 \leftarrow 7}^{1i} \approx 0.2$). The cross sections $Q_{l \leftarrow 7}^\beta$, where $(\{\alpha\}_7, J_7=1)$ is the initial state, closely agree with the $\cos(2\beta)$ dependence of Eq.

(2). For the $(\{\alpha\}_6, J_6=2)$ initial state, the presence of the higher-order $\cos(4\beta)$ term of Eq. (2) is not always immediately apparent (compare, e.g., $Q_{7 \leftarrow 6}^\beta$ with $Q_{4 \leftarrow 6}^\beta$). Of course, much depends on the distribution parameters g_{m_6} .

With our coupled-channel code²⁰ we have calculated polarized cross sections $Q_{l \leftarrow k}^{iM_k}$ for the transitions within the $\text{Ne}^{**}\{\alpha\}_{4,5,6,7}$ multiplet, at some different energies within the experimental energy range. The extended potentials mentioned in Sec. I, which for $R \geq 4.5a_0$ are identical to those of Hennecart and Masnou-Seeuws, were used throughout. Otherwise, the calculations are

similar to those reported before.²⁰ The calculated cross-section values $Q_{l \rightarrow k}^{M_k}$ are compared with those derived from the experiment in Table I. The relevant results for the observed cross sections $Q_{l \rightarrow k}^{\beta}$ [using either Eq. (4) or Eq. (5)] are shown in Figs. 1–3 for the $\{\alpha\}_7 \rightarrow \{\alpha\}_{4,5,6}$ transitions and in Figs. 4–6 for the $\{\alpha\}_6 \rightarrow \{\alpha\}_{4,5,7}$ transitions, together with the experimental results. Agreement between experiment and quantal calculations is observed to be generally good.

For the highly endothermic $\{\alpha\}_7 \rightarrow \{\alpha\}_{4,5}$ and $\{\alpha\}_6 \rightarrow \{\alpha\}_{4,5}$ transitions, in particular, it is necessary to convolute the quantum-mechanical cross-section values with the experimental energy distribution. This is because the measurements yield energy-averaged results. The total center-of-mass energy spread is typically $\Delta E/E \simeq 40\%$, as determined by the velocity distribution of the supersonic primary and secondary beams.²¹ The strong threshold effect in the $\{\alpha\}_7 \rightarrow \{\alpha\}_{4,5}$ transitions ($\Delta E_{75} = -81$ meV, $\Delta E_{74} = -91$ meV) explains why the observed averaged cross sections are much larger than the cross sections which would have been obtained in calculations for the average collision energy. For the $\{\alpha\}_6 \rightarrow \{\alpha\}_{4,5}$ transitions ($\Delta E_{65} = -57$ meV, $\Delta E_{64} = -67$ meV) the threshold effect is less severe. This effect plays a progressively smaller role at the higher energies, at which measurements were performed. For the exothermic transitions, it is generally sufficiently accurate to use the average collision energy in the calculation. In the calculation of effective quantum-mechanical cross sections, generally four or five cross-section values were available within the width of the experimental energy distribution. The convolution procedure was carried out while linearly interpolating between these values.

The experiment offers two methods of varying the Ne^{**}-He collision energy.²⁰ First, by scanning the laser beam along the primary-beam axis, the position of the scattering volume with respect to the secondary-beam nozzle can be varied. The resulting change in the direction of the secondary-beam velocity \mathbf{v}_2 affects both direction and magnitude of the relative velocity \mathbf{g} . Secondly, the magnitude of the primary-beam velocity \mathbf{v}_1 can be changed through the use of a seeding agent. We have used a 15% Ne–85% He seeded primary beam, in addition to a 100% Ne beam.

The observed energy dependence of the $\{\alpha\}_5 \rightarrow \{\alpha\}_{4,6}$ and $\{\alpha\}_7 \rightarrow \{\alpha\}_{5,6}$ cross sections, for which most data are available, is discussed in Sec. IV. Generally speaking, the time-consuming nature of quantum-mechanical coupled-channel calculations is prohibitive, when it comes to simulating the energy dependence of cross sections. In this respect, the semiclassical calculations of Sec. IV are much less demanding.

III. SEMICLASSICAL MODEL

A. Adiabatic representation

To facilitate the discussion, without pretending in any way to provide an overview of semiclassical theory, we now introduce a number of key concepts. The system of nuclei and electrons is described by the wave equation

$$i\hbar \frac{\partial \Psi}{\partial t}(\mathbf{r}, \mathbf{R}, t) = H\Psi(\mathbf{r}, \mathbf{R}, t) = (H_{\text{el}} + T_n)\Psi(\mathbf{r}, \mathbf{R}, t), \quad (6a)$$

$$T_n = T_{\text{rad}} + T_{\text{rot}}, \quad (6b)$$

$$H_{\text{el}} + H_{\text{at}} + V_{\text{mol}}, \quad (6c)$$

in which T_n is the kinetic energy operator of nuclear motion, with T_{rad} and T_{rot} its radial and angular components, and H_{el} is the electronic Hamiltonian, split into the atomic part H_{at} of the separate particles and the remaining molecular part V_{mol} . Within the framework of our scattering problem, we are interested in solutions $\Psi(\mathbf{r}, \mathbf{R})$ of the time-independent Schrödinger equation, where \mathbf{r} represents all electronic coordinates and \mathbf{R} is the internuclear radius vector:

$$(T_n + H_{\text{el}})\Psi(\mathbf{r}, \mathbf{R}) = E\Psi(\mathbf{r}, \mathbf{R}), \quad (7)$$

with E the total energy in the center-of-mass system.

Now, a fully *quantum-mechanical* treatment takes an even-handed approach to the general problem of coupled nuclear-electronic motion. The wave function $\Psi(\mathbf{r}, \mathbf{R})$ is expanded in an orthonormal basis of channel functions, characterized by the collective quantum number i :

$$\Psi(\mathbf{r}, \mathbf{R}) = \sum_i \frac{F_i(R)}{R} |\varphi_i(\mathbf{r}, \mathbf{R})\rangle. \quad (8)$$

The channel functions $|\varphi_i(\mathbf{r}, \mathbf{R})\rangle$ can be written as

$$|\varphi_i(\mathbf{r}, \mathbf{R})\rangle = |\varphi_i(\mathbf{r}'; R)\chi_i(\hat{\mathbf{R}})\rangle, \quad (9)$$

where $\hat{\mathbf{R}} = \mathbf{R}/R$ indicates the orientation of \mathbf{R} , and \mathbf{r}' represents the electronic coordinates \mathbf{r}'_j in the body-fixed frame. The electronic functions $|\varphi_i(\mathbf{r}'; R)\rangle$ depend parametrically on R . Substitution of Eq. (8) into Eq. (7) results in a set of coupled differential equations for the wave functions $F_i(R)$ of radial nuclear motion. In a basis of adiabatic eigenfunctions of the electronic Hamiltonian H_{el} , for which we have

$$H_{\text{el}}|\varphi_i^{\text{ad}}\rangle = (H_{\text{at}} + V_{\text{mol}})|\varphi_i^{\text{ad}}\rangle = V_i(R)|\varphi_i^{\text{ad}}\rangle, \quad (10)$$

nonadiabatic coupling is caused by T_{rad} and T_{rot} .

The *semiclassical* approach to Eq. (7) consists of separating the coupled electronic-nuclear motion into electronic motion, treated quantum mechanically, and nuclear motion, which is now treated classically. Supposing for the moment the latter problem solved, with the classical trajectory $\mathbf{R} = \mathbf{R}(t)$ as a result, we are left with the time-dependent electronic Schrödinger equation

$$i\hbar \frac{\partial \Psi(\mathbf{r}; \mathbf{R}(t))}{\partial t} = H_{\text{el}}(\mathbf{r}, \mathbf{R}(t))\Psi(\mathbf{r}; \mathbf{R}(t)), \quad (11)$$

where the electronic Hamiltonian depends on the time t through the known quantity \mathbf{R} .

In the adiabatic representation of Eq. (10), with the expansion

$$\Psi(\mathbf{r}; \mathbf{R}(t)) = \sum_i a_i(t) |\varphi_i^{\text{ad}}(\mathbf{r}; \mathbf{R}(t))\rangle \times \exp \left[\frac{i}{\hbar} \int^t V_i(\mathbf{R}(t)) dt \right], \quad (12)$$

nonadiabatic coupling is caused by the time-derivative operator

$$-i\hbar \frac{\partial}{\partial t} = -i\hbar \dot{R} \frac{\partial}{\partial R} - i\hbar \dot{\hat{R}} \cdot \frac{\partial}{\partial \hat{R}}. \quad (13a)$$

Taking into account Eq. (9), we have

$$\frac{\partial}{\partial \hat{R}} \Big|_{r=\text{const}} = - \sum_j \frac{\partial}{\partial \hat{r}'_j} \Big|_{\perp} = \frac{1}{i\hbar} \mathbf{J}_{\perp}, \quad (13b)$$

with \perp referring to the component perpendicular to the internuclear z' axis. As a consequence we have

$$-i\hbar \frac{\partial}{\partial t} = -i\hbar v_R \frac{\partial}{\partial R} - \dot{\hat{R}} \cdot \mathbf{J}_{\perp}. \quad (14)$$

Here v_R and $|\dot{\hat{R}}| = \dot{\theta} = \omega$ are the radial and angular velocities of nuclear motion, respectively, θ being the angle of the internuclear axis with the space-fixed z axis, i.e., the polar angle in the collision plane. The operator \mathbf{J}_{\perp} is perpendicular to the collision plane. Given that

$$\mathbf{J}_{\perp} = \frac{1}{2}(\mathbf{J}_{+,z'} + \mathbf{J}_{-,z'}),$$

where $\mathbf{J}_{+,z'}$ and $\mathbf{J}_{-,z'}$ denote the raising and lowering operators for the azimuthal angular momentum $M_{J_z} \hbar$ along the internuclear axis, clearly the terms of Eq. (14) represent radial and rotational nonadiabatic coupling, respectively. In practice, radial coupling will occur mainly between adjacent states k and l within a particular Ω manifold (and reflection symmetry class, for $\Omega=0$). Rotational coupling takes place between different Ω states for a single k , with $|\Omega - \Omega'| = 1$.

Our task will be to find a suitable semiclassical description for both types of coupling, in addition, of course, to working out a solution to the trajectory problem. The calculation of polarized cross sections $Q_{l \leftarrow k}^{M_k}$ for the $(\alpha_k J_k M_{k,z}) \rightarrow (\alpha_l J_l)$ electronic transition calls for a semiclassical transition probability $\mathcal{P}_{l \leftarrow k}^{M_k}(b)$, where b is the impact parameter. For a given \mathcal{P} , it follows directly that

$$Q_{l \leftarrow k}^{M_k} = \int_0^{\infty} 2\pi b \mathcal{P}_{l \leftarrow k}^{M_k}(b) db. \quad (15)$$

Thus it remains to derive a suitable expression for $\mathcal{P}_{l \leftarrow k}^{M_k}$.

B. Radial coupling

Nonadiabatic radial coupling near an avoided crossing of two adiabatic potential curves has first been described semiclassically by the Landau-Zener-Stückelberg (LZS) theory.²⁷⁻²⁹ In its extended LZS form, this model allows for interference between different collision paths followed by a particle, as opposed to the Landau-Zener (LZ) model. A survey of LZS theory is given by Thorson *et al.*³⁰ There have been numerous additions and extensions to LZS theory, notably the inclusion of tunneling effects.^{31,32} At the same time, the application range of previous linear models has been greatly extended by the advent of nonlinear models.^{32,33} For our analysis of Ne** - He intramultiplet mixing, the linear model of Nikitin³¹ has a sufficiently wide application range and offers maximum potential for physical insight.

At the basis of the linear model lies a description of the two-state system near the avoided crossing in terms of only weakly R -dependent diabatic states $|\varphi_k^d\rangle$ and $|\varphi_l^d\rangle$. At a large distance from the crossing these must coincide with the adiabatic states $|\varphi_k^{\text{ad}}\rangle$ and $|\varphi_l^{\text{ad}}\rangle$. For the diabatic matrix elements of H_{el} an approximate expression is adopted, retaining only the linear part of the expansion in terms of $R - R_C$, with R_C the crossing point of the diabatic potential curves $H_{kk}(R)$ and $H_{ll}(R)$:

$$\begin{aligned} H_{kk}(R) &= H_C - F_k(R - R_C), \\ H_{ll}(R) &= H_C - F_l(R - R_C), \\ H_{kl}(R) &= H_{lk}(R) = H_{kl}(R_C) \equiv H_{kl}^{\Omega}, \end{aligned} \quad (16)$$

where $F_j = -(\partial/\partial R)H_{jj}(R)|_{R=R_C}$ is the slope of the diabatic potential at R_C . The crossing point R_C can then be identified as the point of minimum splitting between the adiabatic potentials $V_k^{\Omega}(R)$ and $V_l^{\Omega}(R)$. The crossing potential H_C is given by

$$H_C = [V_k^{\Omega}(R_C) + V_l^{\Omega}(R_C)]/2, \quad (17)$$

while for the coupling-matrix element H_{kl}^{Ω} we find

$$H_{kl}^{\Omega} = [V_k^{\Omega}(R_C) - V_l^{\Omega}(R_C)]/2. \quad (18)$$

This situation is clarified in Fig. 7.

For the total probability P_{kl}^{Ω} of a transition from one adiabatic potential curve to the other, we cite here the limiting case of the original Landau-Zener formula, obtained under the assumption of uniform motion near the crossing radius R_C :

$$P_{kl}^{\Omega} = 2p_{kl}^{\Omega}(1 - p_{kl}^{\Omega}), \quad (19a)$$

$$p_{kl}^{\Omega} = \exp(-v_{kl}^{\Omega}/v_R), \quad (19b)$$

$$v_{kl}^{\Omega} = 2\pi(H_{kl}^{\Omega})^2/\hbar|F_k - F_l|. \quad (19c)$$

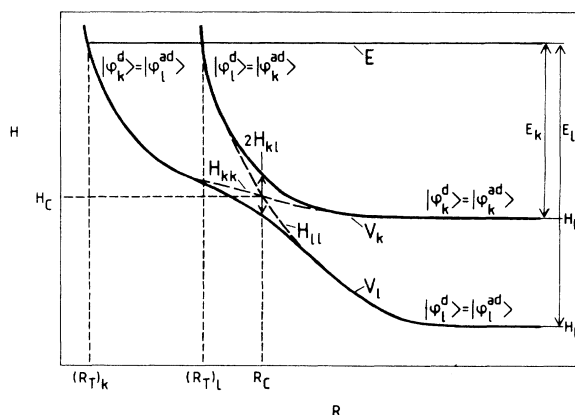


FIG. 7. Schematic picture of an avoided crossing of adiabatic potentials V_k and V_l , with corresponding diabatic potentials H_{kk} and H_{ll} . The crossing parameters of Nikitin's linear model have been indicated, i.e., the crossing point R_C , the crossing energy H_C , and the diabatic coupling matrix element H_{kl} . The non-adiabatic transition probability P_{kl} is determined by the radial energy at the crossing.

Here v_R is the radial velocity, and v_{kl}^{Ω} a reference velocity that contains all information on the coupling at the avoided crossing. In the LZ case, with the crossing radius far from the classical turning point ($R_C \gg R_T$), a transition may occur with single-pass transition probability p_{kl}^{Ω} , both on the incoming and on the outgoing transit. For radial velocities $v_R \ll v_{kl}$, the original adiabatic curve will be *followed* both coming in and going out, whereas for $v_R \gg v_{kl}$, on both occasions a *crossing* to the other curve will take place. In both instances, the total transition probability P_{kl} amounts to zero. A net transition is most likely for intermediate velocities $v_R \approx v_{kl}$. In particular, the maximum value $P_{kl} = \frac{1}{2}$ is obtained for $v_R = v_{kl}/\ln(2)$.

As the classical turning point R_T comes closer to the crossing region ($R_T \lesssim R_C$), interference occurs between incoming and outgoing trajectories. In the general linear model, this is taken into account by postulating constant acceleration by an effective force $F = |F_k F_l|^{1/2}$ near the crossing point. The resulting description is equivalent to the quantum-mechanical one.³⁴ Quantum-mechanical tunneling (important for $R_T \simeq R_C$) is thus simulated as well. The case of F_k and F_l having a different sign, implying transition over or under a potential barrier near the crossing, will not be considered here.

Depending on the coupling strength, the linear model yields analytical expressions $P_{kl}(\epsilon, \beta)$ in certain regions of the (ϵ, β) plane,³¹ with

$$\epsilon = \frac{E_C}{2H_{kl}} \frac{|F_k - F_l|}{|F_k F_l|^{1/2}}, \quad (20)$$

$$\beta = 4H_{kl} \left[\frac{\mu H_{kl}}{\hbar^2 |F_k F_l|^{1/2} |F_k - F_l|} \right]^{1/2}.$$

Of the dimensionless parameters ϵ and β , the first characterizes the (radial) kinetic energy $E_C = \frac{1}{2}\mu v_R^2$ at the crossing point, the second the nonadiabatic coupling-matrix element H_{kl} . The only region for which there is no analytical expression for P_{kl} is defined by $|\epsilon| \approx 1$, $\beta \approx 1$. However, numerically calculated transition probabilities have been tabulated.³⁵

In practice, the centrifugal potential E_{rot} combines with the adiabatic potentials V_k^{Ω} to form effective potentials $V_{\text{eff},k}^{\Omega}(R) = V_k^{\Omega}(R) + E_{\text{rot}}(R)$. Through $E_{\text{rot}} = \frac{1}{2}\mu g^2 b^2 / R^2$, the single-transit and total transition probabilities therefore depend on the impact parameter b (and, of course, on the relative velocity g), and will hereafter be denoted as $p_{kl}^{\Omega}(b)$ and $P_{kl}^{\Omega}(b)$, respectively.

C. Rotational coupling

For polarized cross sections $Q_{l \rightarrow k}^{|M_k|}$ to be determined from the transition probability $P_{kl}^{\Omega}(b)$ of Sec. III B (with $\Omega = |M_k|_{z'}$), it is necessary that the distribution over $M_{k,z'}$ states at the crossing radius R_C be known. The development of a distribution $G_k^{M_{k,z'}}(R)$ from an initial distribution $G_k^{M_{k,z'}}(-\infty) = \delta_{M_{k,z'}, M_k}$ is a matter of nonadiabatic rotational coupling between states $|\alpha_k J_k M_{k,z'}\rangle$ and $|\alpha_k J_k M_{k,z'} \pm 1\rangle$.

The problem of rotational coupling can be reformulated in compliance with the original LZ formalism.³⁶ The dynamical state model³⁷ even enables one to apply LZS theory to cases involving both radial and rotational coupling. In the case of a C_s/R^3 adiabatic potential difference, a different general treatment is possible as well.³⁸ However, for our Ne^{**}-He problem, a somewhat simpler approach is both possible and desirable.

Rotational coupling, of course, simply reflects the effect of describing an essentially space-fixed electronic state in a rotating body-fixed coordinate system. However, it is unrealistic to suppose that the electronic angular momentum \mathbf{J} will retain its space-fixed orientation along the entire trajectory. The “mathematical” rotational coupling must at all times compete with the Ω -conserving “physical” coupling that gave rise to the adiabatic potentials $V_k^{\Omega}(R)$. Their relative importance depends on the magnitude of the Ω splitting

$$\Delta V_k^{\Omega\Omega'}(R) = V_k^{\Omega}(R) - V_k^{\Omega'}(R) \quad (21)$$

compared to the rotational-coupling strength

$$T_{\text{rot}}^{\Omega\Omega'} \simeq [N(N+1)]^{1/2} \hbar^2 / \mu R^2, \quad (22)$$

where $|\Omega - \Omega'| = 1$.

There are two limiting cases to be discerned. If the Ω splitting greatly outweighs the rotational-coupling strength, i.e., if $\Delta V_k^{\Omega\Omega'} \gg T_{\text{rot}}^{\Omega\Omega'}$, the internuclear axis serves as the effective quantization axis and the orientation of the electronic wave function is “locked” to it. For values $\Delta V_k^{\Omega\Omega'} \ll T_{\text{rot}}^{\Omega\Omega'}$, the electronic state observes no angle-dependent forces and remains space fixed. In a semiclassical context, the inherently problematic transition between these extremes is often considered to occur at a fixed position R_L , the so-called locking radius, where the rotational-coupling strength equals the Ω splitting:

$$\Delta V_k^{\Omega\Omega'}(R_L) = f_L [N(N+1)]^{1/2} \hbar^2 / \mu R_L^2. \quad (23)$$

For future reference, we have included here a locking factor f_L .

More insight into the phenomenon of locking than is provided by the above can be obtained from classical mechanics. The Ω splitting $\Delta V^{\Omega\Omega'}$ correlates with an angle-dependent force and thus with a torque, which operates on the spinning top representing the angular momentum \mathbf{J} . The net result of this torque is a precession of \mathbf{J} about the internuclear z' axis, with angular frequency

$$\omega_{\text{prec}} = \Delta V^{\Omega\Omega'} / \hbar. \quad (24)$$

On the other hand, there is the angular velocity of the internuclear axis, due to nuclear motion:

$$\dot{\theta} = [N(N+1)]^{1/2} \hbar / \mu R^2. \quad (25)$$

If $\omega_{\text{prec}} \gg \dot{\theta}$, then \mathbf{J} will precess so rapidly about the internuclear axis as to rotate with it, which implies locking. For $\omega_{\text{prec}} \ll \dot{\theta}$, \mathbf{J} is bound to remain space fixed, since there is hardly time for \mathbf{J} to precess at all during the internuclear axis's rotation from $\theta(-\infty) = 0$ to $\theta(\infty) \simeq \pi$. Defining the onset of locking by $\omega_{\text{prec}} = f_L \dot{\theta}$, we again

find Eq. (23).

It is the spinning-top image of Eqs. (24) and (25), in particular, which suggests the insertion of a locking factor $f_L > 1$ to the right of the equality sign in Eq. (23). For $f_L = 4$, say, we have one full precession of \mathbf{J} for a typical $\theta = \pi/2$ rotation of the internuclear axis.

Another approach is based on the principle of energy conservation. In this case, we have to compare the change of energy for a unity change of the quantum numbers Ω and N , i.e.,

$$\frac{d}{d\Omega} V^\Omega = \Delta V^{\Omega\Omega'} \quad (26)$$

and

$$\frac{d}{dN} E_{\text{rot}} = (N + \frac{1}{2}) \hbar^2 / \mu R^2, \quad (27)$$

where E_{rot} is the rotational energy. If $(d/d\Omega)V^\Omega \gg (d/dN)E_{\text{rot}}$, we expect Ω to be conserved, that is to say locking, since a change in Ω would require an unrealistically large change in N to provide for the necessary change in E_{rot} . Likewise, the condition $(d/d\Omega)V^\Omega \ll (d/dN)E_{\text{rot}}$ means that N must remain unchanged and that rotational coupling will act on the space-fixed \mathbf{J} , changing Ω . With $(d/d\Omega)V^\Omega = f_L (d/dN)E_{\text{rot}}$ and writing $(N + \frac{1}{2}) \simeq [N(N+1)]^{1/2}$, we once more have Eq. (23).

Lastly, as a closing note on locking, we note that the transition from a space-fixed to a body-fixed angular momentum \mathbf{J} corresponds, in the language of molecular spectroscopy, to a transition between Hund's cases "e" and "c."³⁹

The simplification, implicit in the concept of a locking

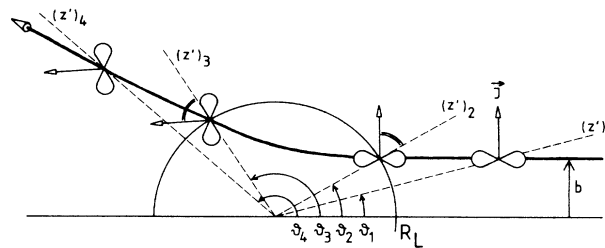


FIG. 8. By introducing a locking radius R_L , we assume the electronic angular momentum \mathbf{J} to be space fixed for $R > R_L$, and locked to the internuclear axis for $R \leq R_L$. Thus we have purely geometrical Ω mixing through rotational coupling for $R > R_L$, and Ω conservation for $R \leq R_L$.

radius, has met with considerable success, e.g., in the $\text{Na}^* + \text{Na}^+$ case.¹⁸ Although this picture of sudden locking, as illustrated by Fig. 8, has proven too simple for $\text{Ne}^{**}\{\alpha\}_9 + \text{Ar}$ collisions,^{2(a)} it is quite appropriate in the present $\text{Ne}^{**}\{\alpha\}_{4,5,6,7} + \text{He}$ context, as will be shown in Sec. III E.

The problem of finding a locking radius has also been discussed by Nikitin,⁴⁰ for the case of small-angle scattering, i.e., large impact parameters. The criterion used for determining R_L is the sufficient accumulation of phase difference between the adiabatic states. For a steep rise of the Ω splitting, this approach will yield results similar to those found by us. We note that, for impact parameters $b \rightarrow 0$, the above so-called "matching" criterion would give a finite value of R_L , whereas in our case $R_L \rightarrow \infty$. However, to the extent that for $b \rightarrow 0$ the space-fixed and body-fixed coordinate systems coincide,

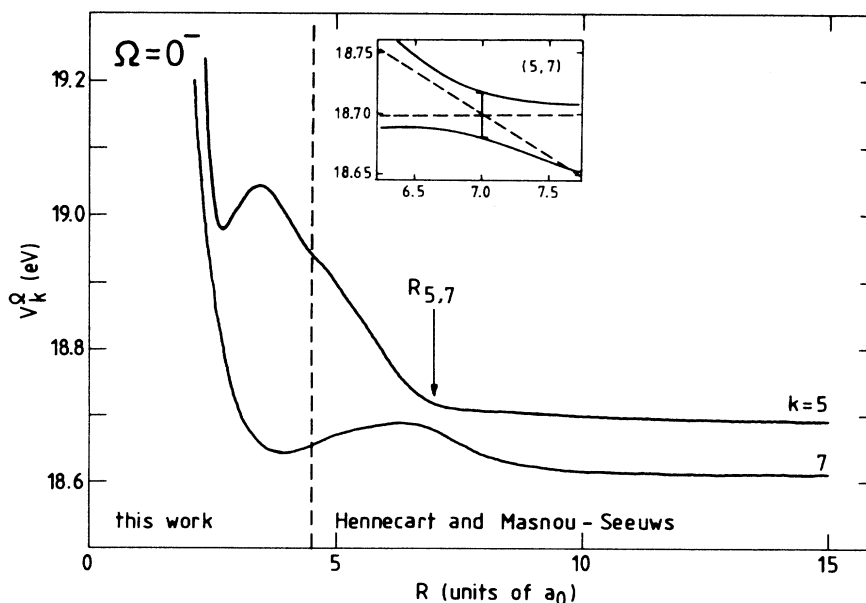


FIG. 9. Adiabatic potential curves $V_k^\Omega(R)$ for $k=5,7$ and $\Omega=0^-$. The arrow points to the position $R_{5,7}$ of the avoided crossing. The inset shows the crossing region in more detail. The diabatic potentials and the coupling-matrix element, indicated in the figure, are given in Table II. See Fig. 7 for comparison.

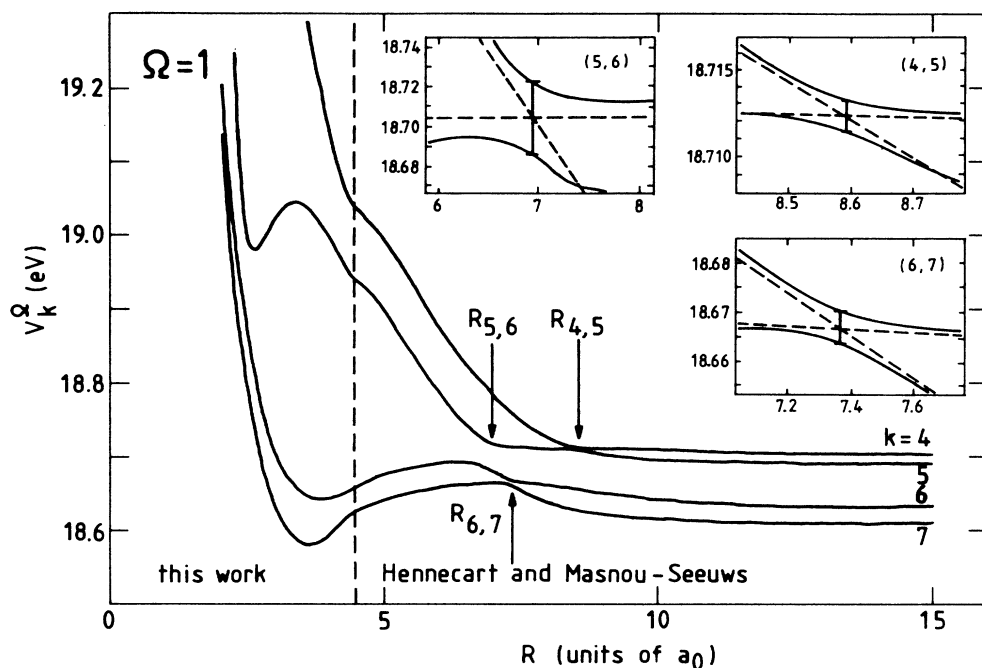


FIG. 10. Adiabatic potential curves $V_k^\Omega(R)$ for $k=4,5,6,7$ and $\Omega=1$. The arrows point to the position $R_{k,l}$ of the avoided crossings. See caption of Fig. 9 for further detail.

the latter is only an artificial effect.

Where locking pertains, the distribution $G_k^\Omega(R)$ over $|\alpha_k J_k(\Omega \equiv |M_k|_{z'})\rangle$ states is bound to remain unchanged. For pure rotational coupling, the effect of a rotation θ_{12} of the internuclear z' axis between two positions $R_1(t_1)$ and $R_2(t_2)$ can be described in terms of the rotation matrices d .²⁶ Given a suitable choice for the x' and y' axes, we may write, with $G_k^{\mathcal{M}}$ the distribution over $\mathcal{M} \equiv M_{k,z'}$,

$$G_k^{\mathcal{M}'}(R_2) = \sum_{\mathcal{M}''} [d_{\mathcal{M},\mathcal{M}''}^J(\theta_{12})]^2 G_k^{\mathcal{M}''}(R_1). \quad (28)$$

Thus, for $J=1$, an initial $\mathcal{M}=0$ state [represented by $G_k^{\mathcal{M}}(R_1) = \delta_{\mathcal{M},0}$] will be mixed according to $G_k^1(R_2) = \sin^2\theta_{12}$ and $G_k^0(R_2) = \cos^2\theta_{12}$, etc.

D. The $\text{Ne}^{**}\text{-He}$ case: avoided crossings

In practice, for $\text{Ne}^{**}\text{-He}$, the various crossing parameters are determined from figures such as Figs. 9 and 10 of the adiabatic potentials, following the guidelines estab-

lished in Sec. III A. The imperfect match to the linear model's assumptions introduces an arbitrary element into the choice of "best" diabatic potentials. Also, the adiabatic potentials themselves, at a given point R_C , are bound to allow small uncertainties. In view of this, it seems appropriate to allow some small realistic latitude in determining optimum effective-diabatic-slope parameters, in particular. In this respect we did not think it necessary to include negative potential slopes. What negative slopes can be constructed are small, the more so if rotational energy is included. Negative slopes would unnecessarily complicate the radial-coupling picture.³¹

The effective-crossing parameters, thus determined, are given in Table II. They correspond to the diabatic potentials and coupling-matrix elements that are indicated in Figs. 9 and 10. All calculations in the present work have used these values. We expressly point out the effect of reflection symmetry, whereby for $\Omega=0^-$ only a single (5,7) avoided crossing is present, as opposed to the three (4,5), (5,6), and (6,7) crossings for $\Omega=1$. Also, it is

TABLE II. Characteristic linear-model parameters for the avoided crossings of the $\{\alpha\}_{4,5,6,7}$ group as shown in Figs. 9 and 10. A broad distinction can be made between crossings with a high and with a low reference velocity v_{kl} . This is instrumental in explaining the observed differences in cross-section behavior. For comparison, the asymptotic energy difference ΔE_{kl} is given as well.

Crossing (k,l)	Ω	R_C (a_0)	H_{kl} (meV)	F_k (meV/ a_0)	F_l (meV/ a_0)	v_{kl} (m/s)	$H_C - H_k$ (meV)	$H_C - H_l$ (meV)	ΔE_{kl} (meV)	$\delta R_C =$ $H_{kl}/\Delta F$ (a_0)
(5,7)	0^-	7.0	20	70	0	2900	6	87	80.6	0.28
(4,5)	1	8.60	0.9	21	0.6	20	9	19	10.7	0.05
(5,6)	1	6.95	17.8	75	0	2150	11	68	56.5	0.24
(6,7)	1	7.35	3.6	42	1.9	165	31	55	24.1	0.09

noteworthy that the reference velocities v_{kl} of the (5,7) and (5,6) crossings on the one hand, and the (4,5) and (6,7) crossings on the other, differ by an order of magnitude.

The values of $H_C - H_k$ in Table II indicate how easily the crossing can be reached. For an estimate of the range of impact parameters b contributing to the cross section for a given initial energy E_k , we must compare the rotational energy at the crossing radius R_C with the total kinetic energy available there. If the crossing is to be reached at all, some radial energy must remain, which gives rise to the following condition for the impact parameter b :

$$\left[\frac{b}{R_C} \right]^2 \leq \frac{E_k - (H_C - H_k)}{E_k}. \quad (29)$$

For positive values of $(H_C - H_k)$, the range is $b < R_C$. Of course, in terms of the classical turning point R_T , Eq. (29) translates to $R_T(b) \leq R_C$.

A closer view of the radial coupling at and near the various avoided crossings of Table II is offered by Fig. 11 of the radial-coupling matrix elements

$$\langle \alpha_l J_l \Omega | \partial / \partial R | \alpha_k J_k \Omega \rangle.$$

In all cases where an avoided crossing of the adiabatic potential curves is present, the corresponding $\partial / \partial R$ -matrix elements display a peak at the crossing radius R_C . This is in contrast with the behavior of a $\partial / \partial R$ -matrix element in the absence of an avoided crossing, exemplified here by the

$$\langle \alpha_3 J_3 \Omega = 0^- | \partial / \partial R | \alpha_4 J_4 \Omega = 0^- \rangle$$

matrix element, which is both smaller and extends over a

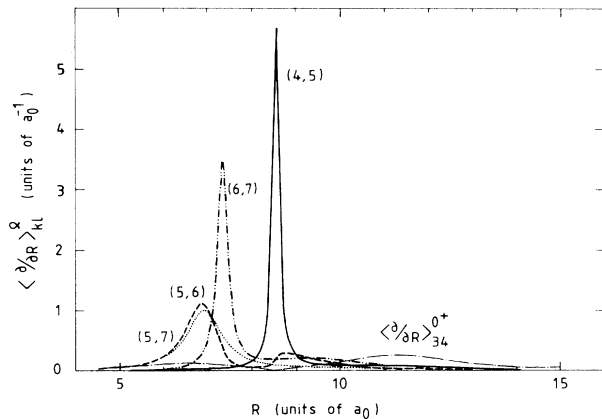


FIG. 11. The radial-coupling matrix element $\langle \alpha_l J_l \Omega | \partial / \partial R | \alpha_k J_k \Omega \rangle$ has a sharp peak, if an avoided crossing of the adiabatic potentials $V_k^{\Omega}(R)$ and $V_l^{\Omega}(R)$ is present. This lies at the basis of our model assumption, that radial coupling is localized at the crossing radius R_C . The matrix element $\langle \alpha_3 J_3 \Omega = 0^+ | \partial / \partial R | \alpha_4 J_4 \Omega = 0^+ \rangle$, which is not associated with an avoided crossing and therefore denoted as $\langle \partial / \partial R \rangle_{34}^{0+}$, extends over a far wider range.

TABLE III. Position R_{\max} , height $\langle \partial / \partial R \rangle_{\max}$, and FWHM width ΔR of the peaks of the radial-coupling matrix elements $\langle \alpha_l J_l \Omega | \partial / \partial R | \alpha_k J_k \Omega \rangle$, associated with the avoided crossings of Table II. The peaks are shown in Fig. 11. See the caption of this figure.

Crossing (k, l)	Ω	R_{\max} (a_0)	$\langle \partial / \partial R \rangle_{\max}$ (a_0^{-1})	ΔR (a_0)
(5,7)	0^-	6.95	1.0	0.95
(4,5)	1	8.55	5.7	0.17
(5,6)	1	6.90	1.1	0.80
(6,7)	1	7.35	3.5	0.27

considerably wider range. The peak values and full widths at half maximum (FWHM) of the $\partial / \partial R$ peaks in Fig. 11 are listed in Table III. By comparison, the maximum value of the

$$\langle \alpha_3 J_3 \Omega = 0^- | \partial / \partial R | \alpha_4 J_4 \Omega = 0^- \rangle$$

matrix element is only $0.25a_0^{-1}$, which still makes it larger than most matrix elements not associated with an avoided crossing. The width of the widest $\partial / \partial R$ peaks is roughly of a size with the minimum wavelengths, encountered at R_C for an initial energy $E = 100$ meV. These are obtained for head-on collisions. For the (5,7) crossing for $\Omega = 0^-$, $E_5 = 100$ meV yields $\lambda_C \leq 0.97a_0$. An energy $E_4 = 100$ meV translates, through multiple curve crossings, to $\lambda_C \leq 0.87a_0$ for the (6,7) crossing for $\Omega = 1$. For $E_6 = 100$ meV, we find for this crossing $\lambda_C \leq 1.12a_0$. This illustrates the localized nature of the avoided crossings.

Comparing Tables II and III, the close relationship between crossing parameters and $\partial / \partial R$ -matrix-element characteristics is obvious. The peak positions R_{\max} are seen to coincide with the crossing radii R_C . The order of magnitude of peak values $\langle \partial / \partial R \rangle_{\max}$ not unexpectedly compares closely to that of the reference velocities v_{kl} . Lastly, the width of the coupling region $\delta R_C = H_{kl} / \Delta F$ (Ref. 31) is directly proportional to the peak width ΔR . In fact, we find approximately $\Delta R \approx 3\delta R_C$.

E. The Ne^{**} -He case: rotational coupling versus locking

In Figs. 12–15 we have plotted the Ω splitting $\Delta V_k^{\Omega\Omega'}$ and the rotational-coupling strength $T_{\text{rot}}^{\Omega\Omega'}(N)$ as a function of the internuclear distance R . From these figures we can determine the locking radius R_L , as defined by Eq. (23). In principle, R_L depends upon the impact parameter b , which is related to the rotational quantum number N by the semiclassical correspondence relation

$$b = (N + \frac{1}{2})\lambda_k, \quad (30)$$

with $\lambda = \hbar / \mu g$ the de Broglie wavelength in the incoming channel. For the Ne^{**} -He system, in practical units, Eq. (30) translates to

$$b = [0.149 \text{ (in units of } a_0)] N (E_k / 100 \text{ meV})^{-1/2}. \quad (31)$$

Equation (23), with locking factor $f_L = 1$, yields lock-

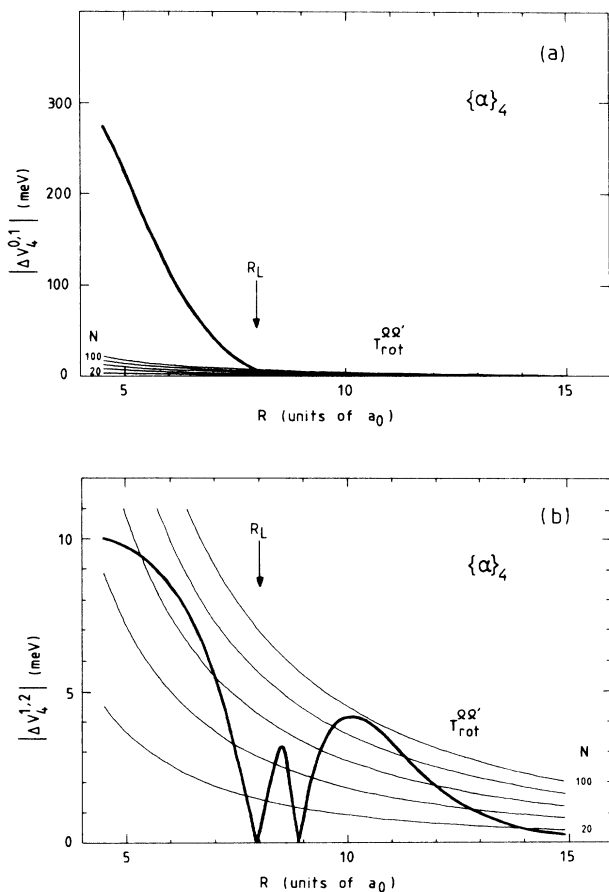


FIG. 12. Ω splitting $\Delta V_k^{\Omega\Omega'}(R)$ of the adiabatic potentials for $k=4$ and $\Omega, \Omega'=0, 1$ (a); $\Omega, \Omega'=1, 2$ (b). Comparison with the rotational-coupling strength $T_{rot}^{\Omega\Omega'}(R)$, in accordance with Eq. (23), offers a criterion for determining a locking radius R_L . The effective locking radius of Table III coincides with the observed steep rise of the Ω splitting.

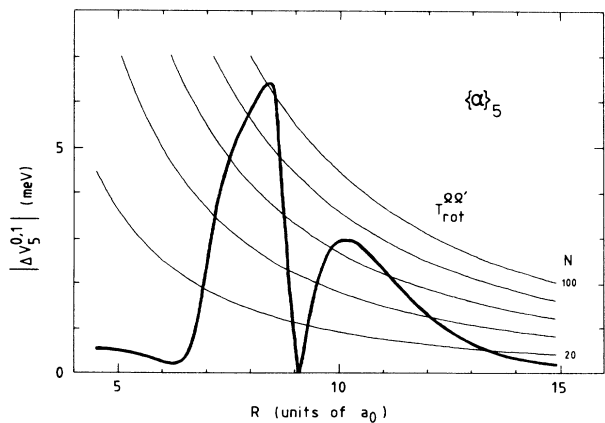


FIG. 13. Ω splitting $\Delta V_k^{\Omega\Omega'}(R)$ for $k=5$ and $\Omega, \Omega'=0, 1$. Locking would seem to occur intermittently. See caption of Fig. 12 for further detail.

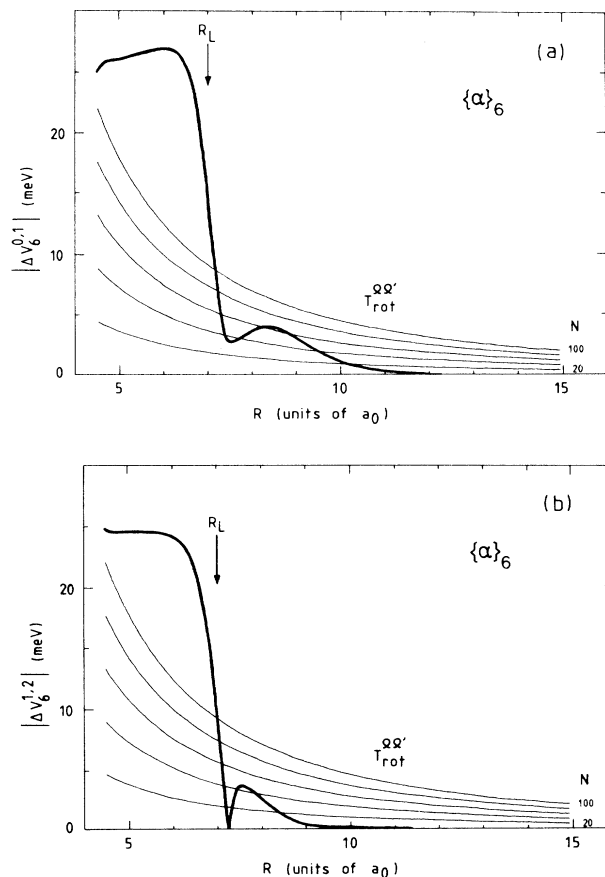


FIG. 14. Ω splitting $\Delta V_k^{\Omega\Omega'}(R)$ for $k=6$ and $\Omega, \Omega'=0, 1$, (a); $\Omega, \Omega'=1, 2$ (b). Note the “hump” at large- R values, which makes it hard to define a single effective locking radius R_L . See caption of Fig. 12 for further detail.

ing radii $R_L(N)$ which are quite far out, especially for low- N values. In fact, at the present thermal energies, they are larger than even the largest crossing radius R_C of Table II over a considerable part of the range of con-

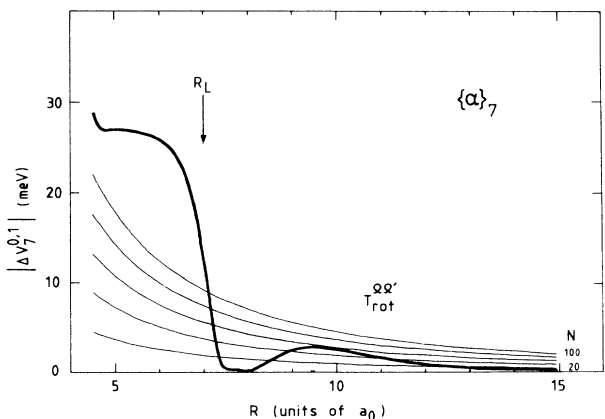


FIG. 15. Ω splitting $\Delta V_k^{\Omega\Omega'}(R)$ for $k=7$ and $\Omega, \Omega'=0, 1$. Once more, it is possible to define an overall locking radius R_L . See caption of Fig. 12 for further detail.

TABLE IV. Effective locking radii R_L for the thermal energy range, deduced from the $\{\alpha\}_{4,5,6,7}$ adiabatic potentials, and approximate values $\Delta V_{k,\max}^{\Omega\Omega'}$ of the Ω splitting at R_L . Rotational coupling may be expected to play a major role in the collision process. In addition, the approximate collision energies E_L are given, at which the concept of a universal locking radius for the states in question must break down, as specified by Eq. (32), with a locking factor $f_L=4$. For $f_L=1$ the values of E_L would be higher by a factor 16.

State k	R_L (a_0)	$\Delta V_{k,\max}^{\Omega\Omega'}$ (meV)	E_L (meV)
4	8.0	22 ^a	220
5			
6	7.1	26	240
7	7.0	24	210

^aValue at $R = 7.5a_0$.

tributing impact parameters. This would effectively negate the role of rotational coupling in bringing about transitions between states $\{\alpha\}_k$ and $\{\alpha\}_l$. It is when postulating a locking factor $f_L \simeq 4$ in Eq. (23) that the steep rise of the Ω splitting with decreasing R enables us to define effective locking radii R_L for the $\{\alpha\}_{4,6,7}$ states, valid for all impact parameters b that contribute to the cross sections of interest. This approach yields the R_L given in Table IV. For the $\{\alpha\}_5$ state, the criterion for locking is met only over a much more limited range of R and N values than for the other states. Since the turning point is always quite far out for this state anyway, we have neglected locking for $\{\alpha\}_5$ altogether. With a single exception, explained later, these are the locking radii which have been used in our calculations.

Looking at Table IV, we observe that locking will occur at a rather large internuclear distance $R = (7-8)a_0$ for all states, except perhaps $\{\alpha\}_5$. Even so, comparison with the crossing radii of Table II shows that in all cases rotational coupling will have its Ω -mixing effect, at least up to or even slightly beyond the various avoided crossings. What consequences this has for the $\{\alpha\}_k \rightarrow \{\alpha\}_l$ cross sections will be discussed in detail in Sec. IV.

At higher initial energies than encountered in this paper, there will be locking only for a limited range of impact parameters $b < R_L$. With the Ω splitting rising steeply at R_L to an approximate value $\Delta V_{k,\max}^{\Omega\Omega'}$, we may perform the following estimate. The energies E_L , for which the locking criterion of Eq. (23) will just barely be met on a trajectory with an impact parameter equal to the locking radii R_L of Table IV, are defined by

$$V_{k,\max}^{\Omega\Omega'} = f_L T_{\text{rot}}^{\Omega\Omega'}(R_L; b = R_L, E = E_L). \quad (32)$$

The values of $\Delta V_{k,\max}^{\Omega\Omega'}$ and the corresponding energy values are given in Table IV as well. It may be concluded that for thermal energies the present concept of a universal locking radius has practical application.

IV. APPLICATION TO THE $\{\alpha\}_{4,5,6,7}$ group

A. Single- and multiple-curve-crossing model

For the calculation of polarized cross sections $Q_{l \leftarrow k}^{|M_k|}$, in accordance with Eq. (15), it remains to combine the concepts of radial coupling and locking and use these with trajectory information in the computation of the total transition probability $\mathcal{P}_{l \leftarrow k}^{|M_k|}$.

As to trajectories, in a discussion of rotational coupling, knowledge of the orientation of the internuclear z axis for any given R (but in particular, of course, for $R = R_C$ and $R = R_L$) clearly is indispensable. Classical trajectories are often assumed to be of constant velocity, and straight lined. While assuming straight-line trajectories, a scattering plane can still be defined by incoming and outgoing relative velocities for a very small scattering angle.¹⁸ All the same, curved trajectories have been used in a semiclassical context.⁴¹ In our present model we will assume scattering from a hard sphere, with radius equal to the (impact-parameter-dependent) classical turning point R_T .

1. Single-curve-crossing model

At the basis of our semiclassical model are a number of approximations and assumptions. Firstly, radial coupling is taken to be strictly localized at the crossing radius R_C . Figure 11 of the

$$\langle \alpha_l J_l \Omega | \partial / \partial R | \alpha_k J_k \Omega \rangle$$

radial-coupling matrix elements lends legitimacy to this assumption, even in the case of the (5,7) matrix element which exhibits the least-pronounced peak. As in Landau-Zener theory, we distinguish between incoming and outgoing transits of the avoided crossing (thus neglecting interference effects). This permits complete separation of radial and rotational coupling. Secondly, there is assumed to be a sharp transition, at the locking

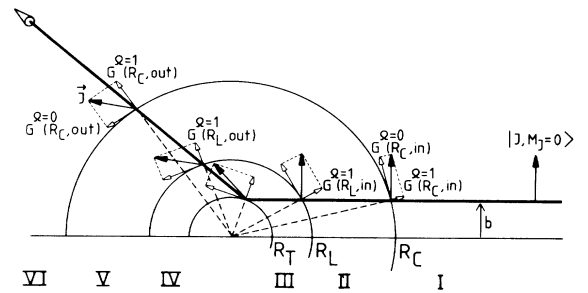


FIG. 16. Overview of the collision process according to the semiclassical model expounded in the text. Indicated are the crossing radius R_C , the locking radius R_L , and the turning point R_T . For $R > R_L$, we have rotational coupling; for $R \leq R_L$, locking. At $R = R_C$ a nonadiabatic transition may take place, both on the incoming and on the outgoing trajectories. The latter are assumed to be straight lined, with hard-sphere scattering at $R = R_T$. We explicitly point out that, for the distribution $G_k^\Omega(R)$ over Ω states, we have $G_k^\Omega(R_C, \text{in}) \neq G_k^\Omega(R_C, \text{out})$, $G_k^\Omega(R_L, \text{in}) = G_k^\Omega(R_L, \text{out})$.

radius R_L , between pure rotational coupling and locking. Justification for this lies in the behavior of the Ω splitting of the adiabatic potentials, as shown in Figs. 12–15. Lastly, in the now disconnected issue of particle trajectories, we postulate hard-sphere scattering at the classical turning point R_T . Of course, at the price of additional computational effort the model could easily accommodate both impact-parameter-dependent locking radii and more realistic trajectories. This was deemed unnecessary, for the moment, in view of various other simplifications inherent to the model.

In the end, for a transition caused by a single avoided crossing, the collision process is as depicted in Fig. 16, where $R_T < R_L < R_C$. On the straight-line incoming trajectory at impact parameter b , we have rotational coupling down to R_C , where the distribution $G_k^{\mathcal{M}}(R)$ over

$$\begin{aligned} P_{kl}^{\mathcal{M}_k|}(b) = & \sum_{\mathcal{M}=-J_k}^{J_k} g_k^{\mathcal{M}_k, \mathcal{M}}(\theta_I) p_{kl}^{\mathcal{M}}(b) \left[\sum_{\mathcal{M}'=-J_l}^{J_l} g_l^{\mathcal{M}, \mathcal{M}'}(\theta_{II} + \theta_V) [1 - p_{kl}^{\mathcal{M}'}(b)] \right] \\ & + \sum_{\mathcal{M}=-J_k}^{J_k} g_k^{\mathcal{M}_k, \mathcal{M}}(\theta_I) [1 - p_{kl}^{\mathcal{M}}(b)] \left[\sum_{\mathcal{M}'=-J_k}^{J_k} g_k^{\mathcal{M}, \mathcal{M}'}(\theta_{II} + \theta_V) p_{kl}^{\mathcal{M}'}(b) \right], \\ g_k^{\mathcal{M}, \mathcal{M}'} = & \{d_{\mathcal{M}, \mathcal{M}'}^{J_k}\}^2, \end{aligned} \quad (33)$$

with $\mathcal{M} \equiv \mathcal{M}_{k,z'}$ or $\mathcal{M} \equiv \mathcal{M}_{l,z'}$, as appropriate.

In cases where LZ theory applies, the appropriate formula yields $p_{kl}^{\mathcal{M}}|$ directly. Otherwise, an effective single-particle transition probability $p_{kl, \text{eff}}^{\mathcal{M}}|$ has been introduced, calculated from the averaged total transition probability $P_{kl}^{\Omega}(\epsilon, \beta)$ of Nikitin, in accordance with Eq. (19a). In the light of our calculation of total (as opposed to differential) cross sections, there is justification for the omission of interference effects implied by this procedure. Of course, for $R_T \simeq R_C$, interference effects once more are fully accounted for, the rotation between R_C and R_T being negligible under the circumstances. Likewise, there is no limitation on tunneling, since this presupposes $R_T \simeq R_C$ anyway. The straight-line trajectories make for a very simple calculation of rotation angles θ .

2. Multiple-curve-crossing model

As is plainly evident from Fig. 10, an $\{\alpha\}_k \rightarrow \{\alpha\}_l$ transition may have to take place via more than one avoided crossing. Of course, the principles expounded in Sec. IV A 1 still apply. Now, we must keep track of all possible particle trajectories, along different adiabatic potentials, with different locking radii R_L and turning points R_T . Every relevant route along the various curve crossings consists of nonadiabatic crossings (probability $p_{kl}^{\mathcal{M}}|$) and adiabatic noncrossings (probability $1 - p_{kl}^{\mathcal{M}}|$). Keeping track of the distribution over $\mathcal{M} \equiv \mathcal{M}_z$ states at each crossing poses a considerable bookkeeping problem. In practice, however, matters may be considerably simplified. Given the relative position of the various avoided crossings and the locking behavior of the states

magnetic substates $\mathcal{M} \equiv \mathcal{M}_{k,z'}$, can be determined. At R_C , each substate may cross from the initial $V_k^{\Omega}(R)$ curve to the $V_l^{\Omega}(R)$ curve, with a transition probability $p_{kl}^{\mathcal{M}}|$. Of course, this implies a probability $(1 - p_{kl}^{\mathcal{M}}|)$ of following the initial curve. The two fractions are then traced separately, once more undergoing rotational coupling down to their respective locking radii R_L , where the angular momentum becomes body fixed, so that the distribution remains constant. At the respective classical turning points R_T , hard-sphere scattering takes place. Then, on the outgoing trajectory, the reverse process evolves.

In view of this, the following expression may be written down for the total probability $P_{l \leftarrow k}^{\mathcal{M}_k|}$ of a transition from the polarized $|\alpha_k J_k \mathcal{M}_k\rangle$ state to the $|\alpha_l J_l\rangle$ state (the Roman numerals denote the various R regions in Fig. 16):

involved (see Tables II and IV), the interaction between the $\Omega=0^-$ and 1 manifolds is bound to be minimal, in the $\text{Ne}^{**}\text{-He}$ case. Our calculations have therefore been limited to a single Ω manifold at a time. Otherwise, all effects of rotational coupling have been properly accounted for.

A cross-section calculation for a single energy at present takes only about 30 sec on an AT-compatible microcomputer with numerical coprocessor. This contrasts sharply with the 2–3 hours on a Burroughs B7900 mainframe computer, required by every quantum-mechanical calculation,²⁰ which translates to 30–45 h on the AT-compatible microcomputer.

B. The $\{\alpha\}_5 \leftrightarrow \{\alpha\}_7$ transitions

The $\{\alpha\}_5 \leftrightarrow \{\alpha\}_7$ transitions are governed almost exclusively by the (5,7) avoided crossing for $\Omega=0^-$. The greatly disparate reference velocities of the (4,5), (5,6), and (6,7) crossings for $\Omega=1$ make a multiple-curve-crossing $\{\alpha\}_5 \leftrightarrow \{\alpha\}_7$ transition unlikely. The high reference velocity $v_{57}^{\Omega=0}$ implies a main cross-section contribution from small impact parameters, where radial velocities are large (“head-on” collisions). Even without locking, the initial Ω orientation will then be largely conserved at the crossing, hence the large polarization effect $Q_{7 \leftarrow 5}^{[0]} \gg Q_{7 \leftarrow 5}^{[1]}$ in the $\{\alpha\}_5 \rightarrow \{\alpha\}_7$ cross sections. With $\{\alpha\}_7$ as initial state, the radial energy at the crossing is less than with $\{\alpha\}_5$. So, the main contribution to the $\{\alpha\}_7 \rightarrow \{\alpha\}_5$ cross section will come from even smaller impact parameters than in the $\{\alpha\}_5 \rightarrow \{\alpha\}_7$ case [Eq. (29)]. This translates to both a smaller $\{\alpha\}_7 \rightarrow \{\alpha\}_5$ cross

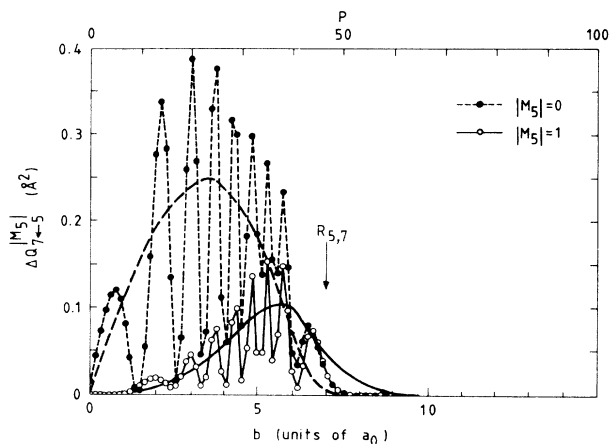


FIG. 17. Semiclassical cross-section contributions $dQ_{7-5}^{M_5}(b)/db$, as a function of the impact parameter b , at energy $E_5=100$ meV. The dashed line (---) represents $|M_5|=0$, the solid line (—), $|M_5|=1$. They compare closely with their quantum-mechanical analogues $\Delta Q_{7-5}^{M_5}(P)$, indicated by filled circles (●) for $|M_5|=0$, and open circles (○) for $|M_5|=1$. Fairly small impact parameters are preferred, yielding a large orientation effect. The arrow points to the avoided-crossing position $R_{5,7}$.

section and a larger polarization effect.

The above is illustrated by Figs. 17 and 18, which compare semiclassical cross-section contributions $dQ_{5-7}^{M_k}(b)/db$ with their quantum-mechanical counterparts $\Delta Q_{5-7}^{M_k}(P)$ at an initial energy $E=100$ meV. For this, we have made use of the correspondence relation of Eq. (30) and approximated the total angular momentum by $P \simeq N$. Averaging out the interference oscillations in the quantum-mechanical cross-section contributions brings out the excellent agreement with the semiclassical

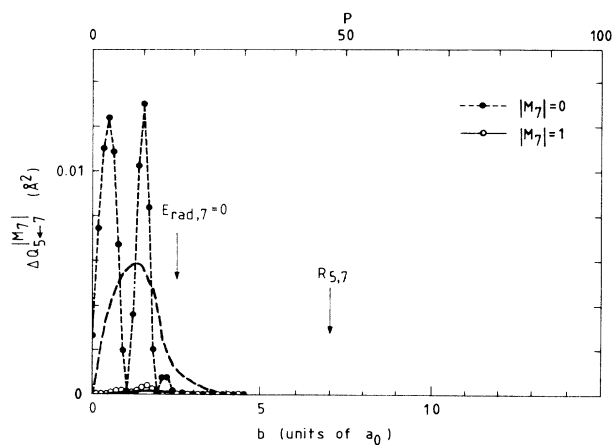


FIG. 18. Semiclassical and quantum-mechanical cross-section contributions $dQ_{5-7}^{M_7}(b)/db$ and $\Delta Q_{5-7}^{M_7}(P)$, at energy $E_7=100$ meV. The endothermic nature of the transition dictates a preference for even smaller impact parameters than in the case of the reverse transition of Fig. 17. See caption of Fig. 17 for further detail.

results. This holds both for the general behavior, and for the position of the maximum. The preferred head-on character of the collision is evident at once.

Figures 19 and 20 show the energy dependence of the semiclassical polarized-atom cross sections $Q_{7-5}^{M_5}$ and $Q_{5-7}^{M_7}$, together with the experimental cross sections. The latter are seen to rise with the energy, as do all cross sections studied in the present paper. The initial rise of the polarization effect with falling energy reflects the effective Ω conservation implied by a shift to smaller impact parameters. Agreement between semiclassical theory and experiment is good. The same can be said regarding the results of the quantum-mechanical calculations, performed with our coupled-channel code.

The experimentally observed threshold behavior of the cross sections for endothermic transitions is obscured to a certain extent by the fact that average velocities only are considered here. The calculated energy spread of about $\Delta E \simeq 40$ meV, due to the primary- and secondary-beam (Gaussian) velocity distributions and to the spatial extent of the scattering volume,²¹ roughly corresponds with the

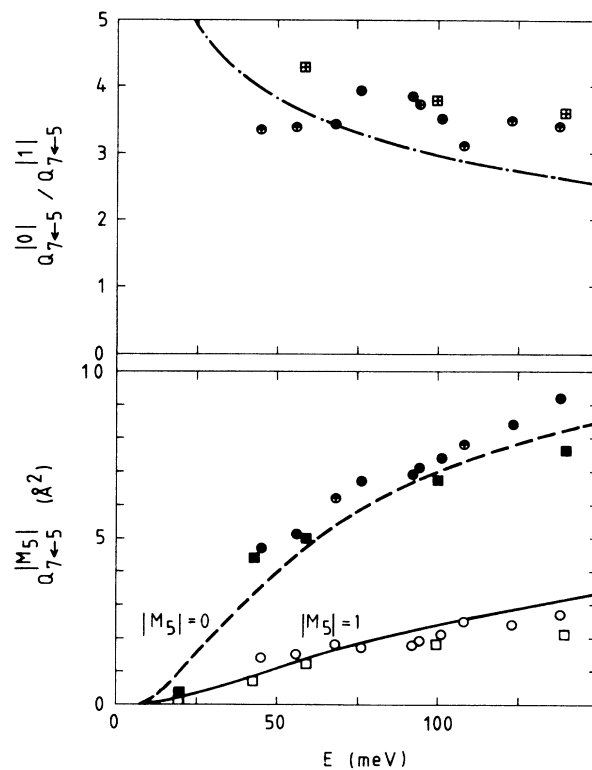


FIG. 19. Energy dependence of the polarized cross sections Q_{7-5}^{10} and Q_{7-5}^{11} , with E the center-of-mass energy. Filled (●) and open (○) circles depict the experimental data points, dashed (---) and solid (—) lines the semiclassical results. In addition, three quantum-mechanical cross sections are shown, indicated by filled (■) and open (□) quadrangles. (All for $|M_5|=0$ and 1, respectively.) The corresponding polarization effect $Q_{7-5}^{10}/Q_{7-5}^{11}$ is given as well, in a similar notation. For $E=43$ meV, the quantum-mechanical polarization effect has a value of 6.3.

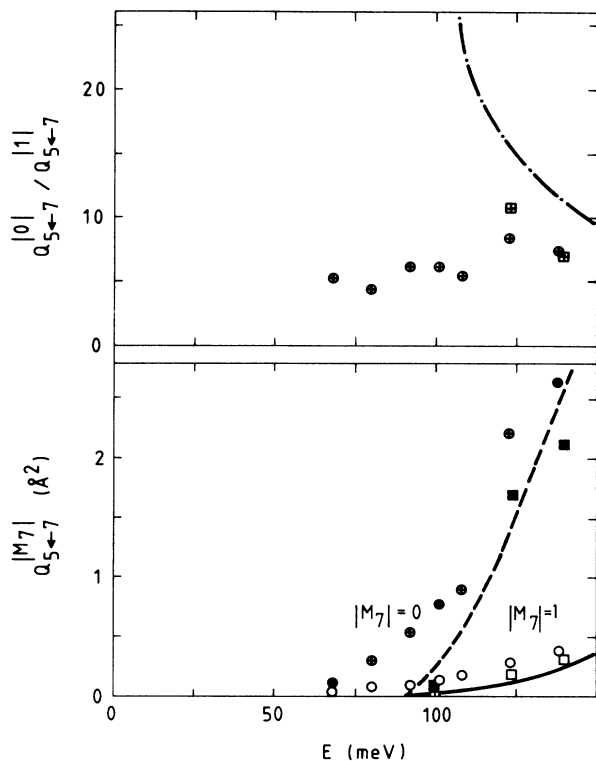


FIG. 20. Energy dependence of the polarized cross sections $Q_{5\leftarrow 7}^{0|}$ and $Q_{5\leftarrow 7}^{1|}$. The behavior of the experimental data points near the threshold energy $E = \Delta E_{57} = 91$ meV is strongly influenced by the experimental velocity distribution which, as no data averaging has been applied here, makes the comparison with the semiclassical and quantum-mechanical cross sections break down. For $E = 100$ meV, the quantum-mechanical polarization effects has a value of 30. See caption of Fig. 19 for further detail.

observed transgression of the energy threshold. These convolution effects have not been included here, other than (where necessary) in Table I and Figs. 1–6.

C. The $\{\alpha\}_5 \leftrightarrow \{\alpha\}_4$ transitions

The $\{\alpha\}_5 \rightarrow \{\alpha\}_4$ transition is caused in effect by the isolated (4,5) avoiding crossing for $\Omega = 1$, which has a low reference velocity $v_{45}^{\Omega=1} \approx 20$ ms⁻¹. The small radial velocities, required for optimum coupling, imply that at the high-velocity inner (5,6) avoided crossing almost always the adiabatic curve is followed. For the favored larger impact parameters (“glancing” collisions), Ω mixing up to the crossing point R_C is considerable. The absence of locking on the $\{\alpha\}_5$ curve leads to an even more thorough Ω mixing and to the virtual absence of a polarization effect: $Q_{4\leftarrow 5}^{0|} \approx Q_{4\leftarrow 5}^{1|}$. The small asymptotic energy difference $\Delta E_{45} = 11$ meV results in calculated cross sections for the endothermic $\{\alpha\}_4 \rightarrow \{\alpha\}_5$ transition, which are only slightly smaller than the $\{\alpha\}_5 \rightarrow \{\alpha\}_4$ cross sections.

The $\{\alpha\}_5 \rightarrow \{\alpha\}_4$ transition is very instructive in several regards. First of all, it is rotational coupling that

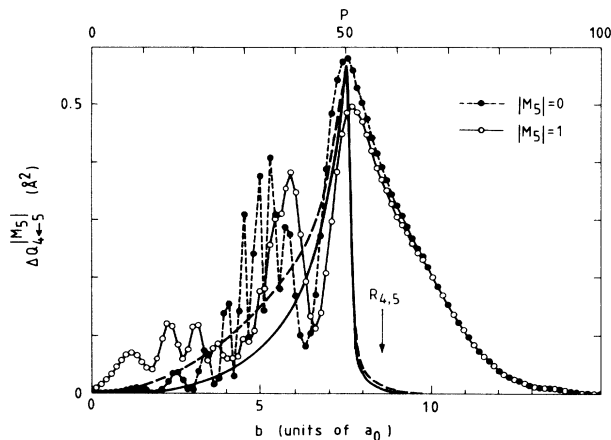


FIG. 21. Semiclassical and quantum-mechanical cross-section contributions $dQ_{4\leftarrow 5}^{M_5}(b)/db$ and $\Delta Q_{4\leftarrow 5}^{M_5}(P)$, at energy $E_5 = 100$ meV. The preference for intermediate impact parameters combined with the absence of locking on the $\{\alpha\}_5$ curve, leads to thorough Ω mixing and almost no overall polarization effect. The semiclassical cross-section contributions are cut off when the turning point passes the crossing radius. The quantum-mechanical large-impact-parameter contributions point to an additional radial-coupling mechanism. See caption of Fig. 17 for further detail.

is largely responsible for the transition. The peculiar nature of the (4,5) crossing, with its extremely low reference velocity $v_{45}^{\Omega=1} \approx 20$ ms⁻¹, makes the single-transit crossing probability close to unity. For a net transition to take place, rather than two subsequent crossings, rotational coupling is required to generate an $|M_4|_{z'} \neq 1$ component, which cannot cross again at the second transit. Of course, rotation of the $|M_5|_{z'} \neq 1$ components at the first transit of the avoided crossing to $|M_5|_{z'} = 1$ at the second transit has a similar effect. For this reason, the expected

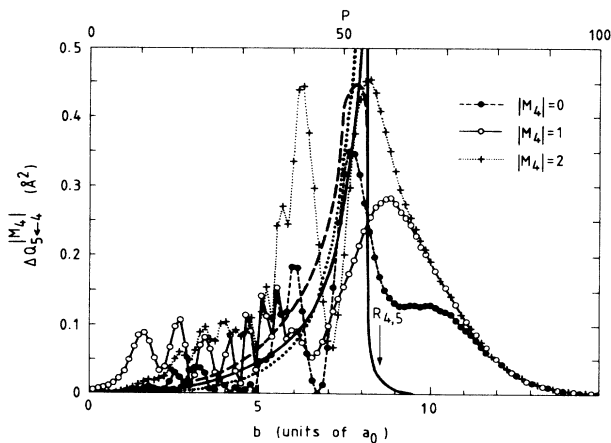


FIG. 22. Semiclassical and quantum-mechanical cross-section contributions $dQ_{5\leftarrow 4}^{M_4}(b)/db$ and $\Delta Q_{5\leftarrow 4}^{M_4}(P)$, at energy $E_4 = 100$ meV. The similarity to Fig. 21 is not surprising in view of the small energy difference ΔE_{45} . See caption of Fig. 17 for further detail.

Landau-Zener pattern of a rise and subsequent fall of the cross sections does not materialize. To the $\{\alpha\}_4 \rightarrow \{\alpha\}_5$ crossing, the same reasoning can be applied. With locking radii equal to the crossing radius, we would obtain cross sections $Q_{4 \leftarrow 5}^{|M_5|}, Q_{5 \leftarrow 4}^{|M_4|} < 1 \text{ \AA}^2$, at $E_5 = 100 \text{ meV}$. This both confirms the need for a locking factor $f_L \gtrsim 1$ in Eq. (23), and provides a quite accurate upper limit for the locking radii in question. Rotational coupling inside of the inner (5,6) avoided crossing turns out to play no part. It is possible to represent this crossing as a simple loss term on the $\{\alpha\}_5$ curve, due to radial coupling only.

A second interesting aspect of the $\{\alpha\}_5 \rightarrow \{\alpha\}_4$ transition is evident from Fig. 21, which once more compares semiclassical and quantum-mechanical cross-section contributions per impact-parameter value, for $E_5 = 100 \text{ meV}$. Agreement is good, up to the sharp cutoff in the semiclassical cross sections that signals the onset of tunneling at the turning point. This behavior, closely paralleled by that for the $\{\alpha\}_4 \rightarrow \{\alpha\}_5$ transition in Fig. 22, is quite insensitive to the (4,5)-crossing-parameter values. To account for the quantum-mechanical contributions at large impact parameters, a different radial-coupling mechanism seems to be required.

The $\{\alpha\}_5 \rightarrow \{\alpha\}_4$ transition thus appears to be a prime candidate for the tentative demonstration of Demkov coupling.⁴² This is supported by Fig. 23 of the development of the mixing angle $\gamma_k^\Omega(R)$ between the adiabatic eigenfunctions

$$|\alpha_k J_k \Omega = 1 (R = \infty)\rangle$$

and

$$|\alpha_k J_k \Omega = 1 (R)\rangle,$$

for $k=4,5$. Ideally, a Landau-Zener-type avoided crossing involves a $\pi/2$ rotation of the adiabatic eigenfunctions, while a $\pi/4$ rotation is associated with Demkov

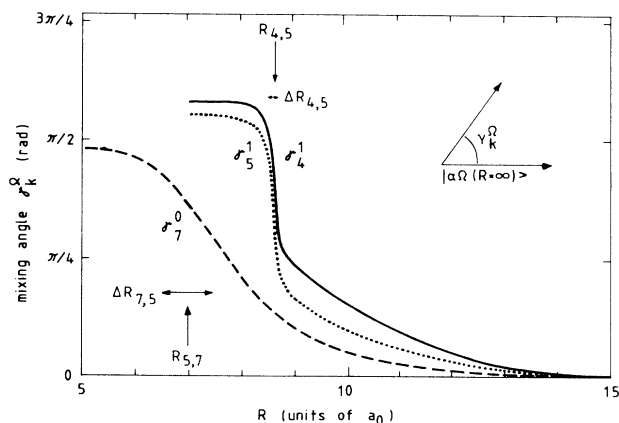


FIG. 23. Development with decreasing R of the mixing angle $\gamma_k^\Omega(R)$ between adiabatic eigenfunctions $|\alpha_k J_k \Omega_k (R = \infty)\rangle$ and $|\alpha_k J_k \Omega_k (R)\rangle$, with $k=4,5$ for $\Omega=1$, and $k=7$ for $\Omega=0$. For $k=4,5$ the effect of the (4,5) avoided crossing is added to by a substantial rotation for large- R values. This reflects additional radial coupling, perhaps of Demkov type.

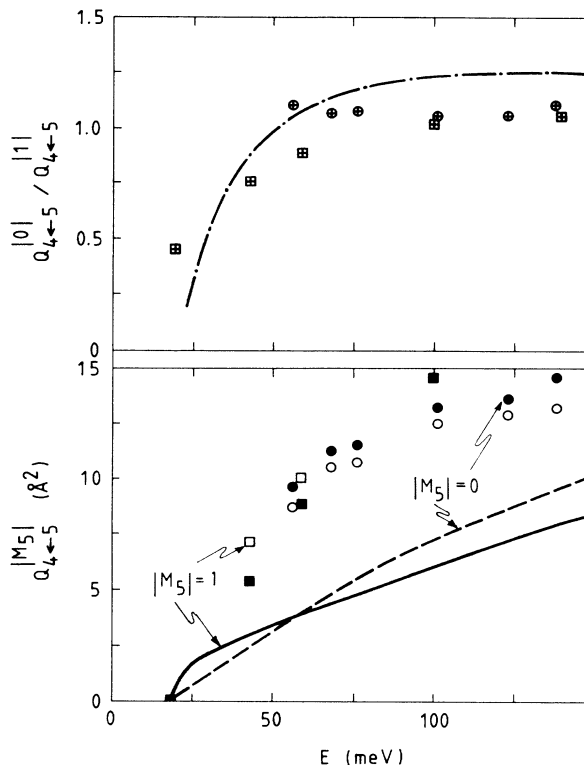


FIG. 24. Energy dependence of the polarized cross sections $Q_{4 \leftarrow 5}^{|0|}$ and $Q_{4 \leftarrow 5}^{|1|}$. Added radial coupling may explain the discrepancy between semiclassical and quantum-mechanical (and experimental) cross sections. See caption of Fig. 19 for further detail.

coupling. Whereas obviously neither case applies here with textbook clarity, the influence of the (4,5) avoided crossing for $\Omega=0$ is unmistakable. The sharp transition near the (4,5) crossing radius $R_C = 8.6a_0$ makes the gradual rotation over close to $\pi/4$ in the outer R regions the more remarkable. Compare this, in the same figure, with the much smaller amount of mixing displayed by the $|\alpha_7 J_7 \Omega=0 (R)\rangle$ state, in spite of the more diffuse character of the (5,7) avoided crossing for $\Omega=0$.

We must look at Fig. 24, which shows the semiclassically calculated energy dependence of the $Q_{4 \leftarrow 5}^{|M_5|}$ cross sections, with the above in mind. What differences with the quantum-mechanical cross sections there are, stem mainly from a lack of large-impact-parameter contributions. In our opinion the conclusion is justified that the $\{\alpha\}_5 \rightarrow \{\alpha\}_4$ transition is essentially caused by Demkov coupling in the outer R regions and LZ coupling at R_C .

The quantum-mechanical calculations, in their turn, agree well with the experimental results. Lower energies (and smaller impact parameters) in this case favor the $\Omega=|1|$ cross section, which means a decreasing polarization effect. As yet, there are no experimental data for the $\{\alpha\}_4 \rightarrow \{\alpha\}_5$ transition.

D. The $\{\alpha\}_{7 \leftrightarrow 6}$ transitions

The $\{\alpha\}_{7 \leftrightarrow 6}$ transitions are caused mainly by the (6,7) avoided crossing for $\Omega=1$. It resembles the (4,5)

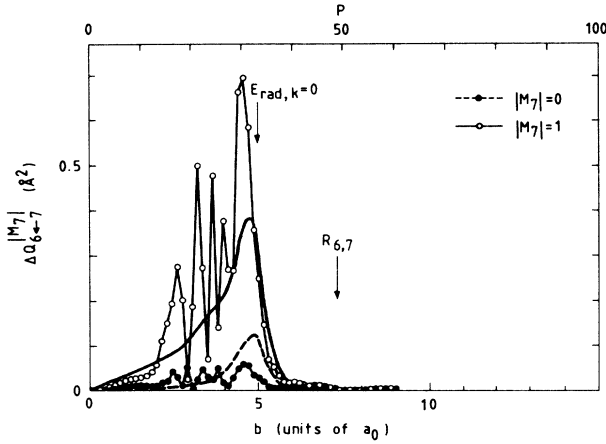


FIG. 25. Semiclassical and quantum-mechanical cross-section contributions $dQ_{6\leftarrow 7}^{M_7}(b)/db$ and $\Delta Q_{6\leftarrow 7}^{M_7}(P)$, at energy $E_7=100$ meV. See caption of Fig. 17 for further detail.

crossing in the same Ω manifold, but has not quite so small a reference velocity. Also, of course, the crossing radius is smaller. Other than for the $\{\alpha\}_5 \leftrightarrow \{\alpha\}_4$ transitions, however, on account of more complete locking in the inner regions there is a remaining orientation effect for the $\{\alpha\}_7$ initial state: $Q_{6\leftarrow 7}^{11} > Q_{6\leftarrow 7}^{01}$. For the $\{\alpha\}_6$ initial state, the energy at the crossing is larger than for the $\{\alpha\}_7$ state, thereby forcing impact parameters to be larger still (“grazing” collisions). In fact, even a small inversion of the polarization effect is observed: $Q_{7\leftarrow 6}^{11} \lesssim Q_{7\leftarrow 6}^{01}$, though, of course, here there is a $Q_{7\leftarrow 6}^{21}$ cross section to be taken into account as well ($J_6=2$).

For the $\{\alpha\}_7 \rightarrow \{\alpha\}_6$ transition, semiclassical cross-section behavior as a function of the impact parameter, at energy $E_7=100$ meV, compares favorably with that of the quantum-mechanical cross sections, as may be seen from Fig. 25. Figure 26 for the reverse $\{\alpha\}_6 \rightarrow \{\alpha\}_7$ transition, at $E_6=100$ meV, also displays good agreement.

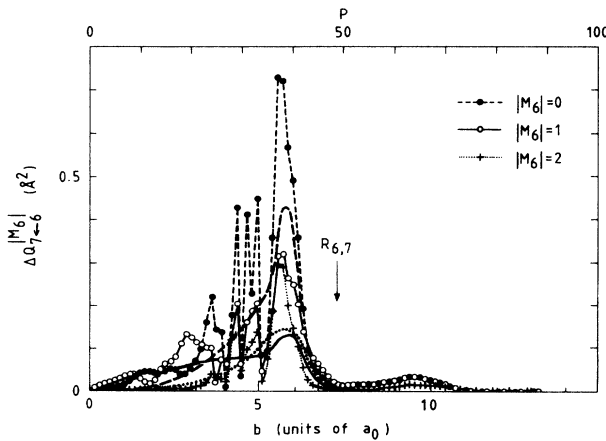


FIG. 26. Semiclassical and quantum-mechanical cross-section contributions $dQ_{7\leftarrow 6}^{M_6}(b)/db$ and $\Delta Q_{7\leftarrow 6}^{M_6}(P)$, at energy $E_6=100$ meV. See caption of Fig. 17 for further detail.

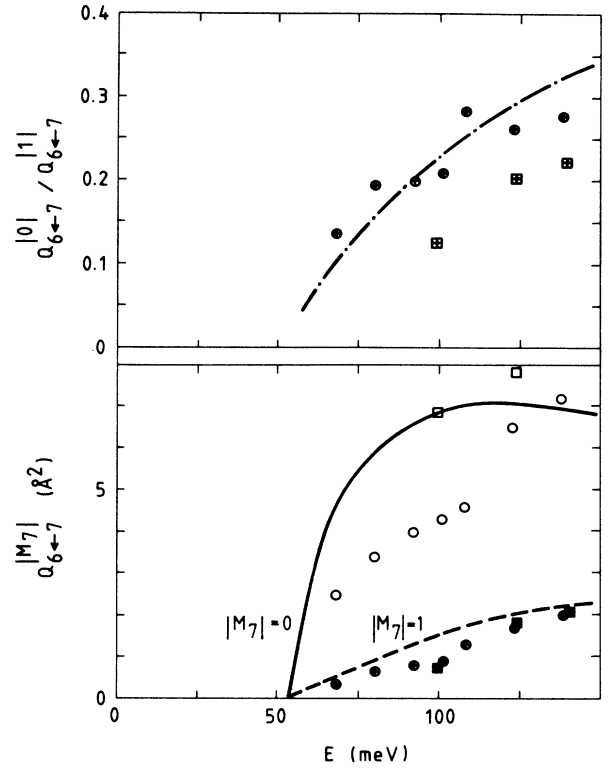


FIG. 27. Energy dependence of the polarized cross sections $Q_{6\leftarrow 7}^{01}$ and $Q_{6\leftarrow 7}^{11}$. Other than the experimental and quantum-mechanical cross sections, the semiclassical cross sections fall off with rising energy. A reference velocity for the (6,7) avoided crossing, sufficiently large to change this, is unlikely. For $E=140$ meV, we find $Q_{6\leftarrow 7}^{11}=9.7 \text{ \AA}^2$, quantum mechanically. See caption of Fig. 19 for further detail.

The $\{\alpha\}_7 \rightarrow \{\alpha\}_6$ polarization effect is underestimated, though. Some improvement may be achieved by using a larger effective locking radius for the $\{\alpha\}_7$ state than indicated in Table IV. The larger value, $R_L=9.0a_0$, perhaps reflects the slowly rising flank of the Ω splitting $\Delta V_{7,1}^{0,1}$ in Fig. 15. No realistic change in crossing parameters, though, can correct the tendency of the semiclassical cross sections $Q_{6\leftarrow 7}^{M_6}$ to decrease prematurely with rising energy (in contrast to the cross section $Q_{4\leftarrow 5}^{M_5}$), as shown in Fig. 27. The $\{\alpha\}_6 \rightarrow \{\alpha\}_7$ transition has only been measured at a single energy, so far.

E. The $\{\alpha\}_5 \leftrightarrow \{\alpha\}_6$, $\{\alpha\}_7, 6 \leftrightarrow \{\alpha\}_4$ transitions

Transitions $\{\alpha\}_{4,5} \leftrightarrow \{\alpha\}_{6,7}$ are possible only through multiple curve crossings. The high radial velocities favored by the inner (5,6) crossing imply a dominant contribution from small impact parameters. In view of the locking on all but the $\{\alpha\}_5$ curve, some polarization effect is to be expected. For high radial velocities, a single-transit nonadiabatic transition is much more likely at the low-velocity (4,5) and (6,7) crossings than single-transit adiabatic following. The $\{\alpha\}_4 \rightarrow \{\alpha\}_7$ transition is therefore the most probable, with cross sections comparable

TABLE V. Performance of the semiclassical model. Comparison of semiclassical and quantum-mechanical polarized total cross sections $Q_{l \rightarrow k}^{M_k}$, at center-of-mass energy $E=100$ meV of the initial state $\{\alpha\}_k$.

Initial state $\{\alpha\}_k$	Final state $\{\alpha\}_l$	Cross section $(Q_{l \rightarrow k}^{M_k})_{SC}/(Q_{l \rightarrow k}^{M_k})_{QM}$			Polarization effect $(Q_{l \rightarrow k}^{0l}/Q_{l \rightarrow k}^{1l})_{SC}/(Q_{l \rightarrow k}^{0l}/Q_{l \rightarrow k}^{1l})_{QM}$
		$ M_k =0$	$ M_k =1$	$ M_k =2$	
$\{\alpha\}_4$	$\{\alpha\}_5$	1.4	1.1	0.7	1.3
	$\{\alpha\}_6$	0.4	0.4	0.3	1.0
	$\{\alpha\}_7$	2.6	2.1	1.8	1.2
$\{\alpha\}_5$	$\{\alpha\}_4$	0.8	0.8		1.0
	$\{\alpha\}_6$	0.02	0.07		0.3
	$\{\alpha\}_7$	1.0	1.2		0.8
$\{\alpha\}_6$	$\{\alpha\}_4$	0.6	0.5	0.7	1.3
	$\{\alpha\}_5$	1.0	0.2	0.8	10
	$\{\alpha\}_7$	0.8	0.7	1.3	1.2
$\{\alpha\}_7$	$\{\alpha\}_4$	0.2	1.1		0.13
	$\{\alpha\}_5$	2.5	2.3		1.1
	$\{\alpha\}_6$	1.8	1.0		1.8

even to those for the single-curve-crossing transitions. Once again, we expect more of an orientation effect in the reverse highly endothermic ($\Delta E_{74} = -91$ meV) $\{\alpha\}_7 \rightarrow \{\alpha\}_4$ transition, for the same initial energy. Figure 28, which compares the composition of semiclassical and quantum-mechanical cross sections for the $\{\alpha\}_4 \rightarrow \{\alpha\}_7$ transition, once more at initial-state energy $E_4 = 100$ meV, shows them to be in reasonable agreement.

The transitions requiring adiabatic following at one ($\{\alpha\}_4 \leftrightarrow \{\alpha\}_6$ and $\{\alpha\}_5 \leftrightarrow \{\alpha\}_7$) or both ($\{\alpha\}_5 \rightarrow \{\alpha\}_6$) of the (4,5) and (6,7) crossings are progressively less likely than the $\{\alpha\}_4 \leftrightarrow \{\alpha\}_7$ transitions. This is roughly the behavior displayed by the quantum-mechanical cross sec-

tions of Table I. The smaller the cross sections, the sooner our simple semiclassical model may be expected to deviate from quantum-mechanical "reality." Even here, though, qualitative agreement is sometimes maintained, as, e.g., for the $\{\alpha\}_6 \rightarrow \{\alpha\}_4$ transition. On the other hand, while, e.g., the $\{\alpha\}_5 \rightarrow \{\alpha\}_6$ quantum-mechanical cross sections are small, the semiclassical cross sections are considerably smaller still and cannot be said to present a true picture anymore. Once more, this may indicate radial-coupling mechanisms not included in our model. For none of these transitions are experimental energy-dependence data available.

For the transitions of this subsection and for all transitions discussed earlier, Table V offers a comparison between semiclassical and quantum-mechanical *total* cross sections. Some possible reasons for existing discrepancies have been given above. In general, though, the quantum-mechanical results are qualitatively and often quantitatively reproduced by the calculations with our semiclassical model. We note that by fitting the semiclassical crossing parameters to the cross-section data, still better agreement could have been obtained.

F. General conclusions

From the previous case studies, several general conclusions may be drawn as to cross-section magnitude, dominance of impact-parameter regions, and polarization effects. First, for two adjacent $\{\alpha\}$ states, an isolated avoided crossing between the adiabatic potentials will result in large cross sections. This is true when only a single crossing is present, but also when the principal crossing is "isolated" by a second, inner crossing with an entirely different reference velocity and thus representing only a small loss term. In comparison with transitions outside the $\{\alpha\}_{4,5,6,7}$ multiplet,²⁰ the cross sections that meet the above criterion (i.e., the $\{\alpha\}_5 \leftrightarrow \{\alpha\}_7$, $\{\alpha\}_5 \leftrightarrow \{\alpha\}_4$, and $\{\alpha\}_7 \leftrightarrow \{\alpha\}_6$ cross sections) are indeed

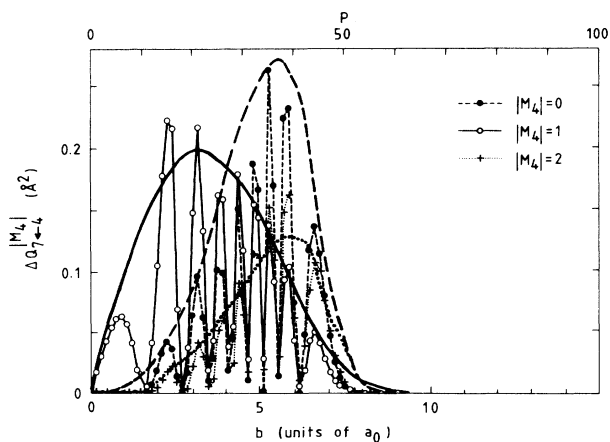


FIG. 28. Semiclassical and quantum-mechanical cross-section contributions $dQ_{7 \rightarrow 4}^{M_4}(b)/db$ and $\Delta Q_{7 \rightarrow 4}^{M_4}(P)$, at energy $E_4 = 100$ meV. The large crossing probabilities p_{kl} at the outer (4,5) and (6,7) avoided crossings make this multiple-curve-crossing transition quite likely, thus the large cross sections. See caption of Fig. 17 for further detail.

relatively large. The same principle, in reverse, holds for the true multiple-curve-crossing transitions. Here, the inner of three crossings determines the preferred velocity. Hence the $\{\alpha\}_6 \rightarrow \{\alpha\}_4$ cross section is bound to be larger than the $\{\alpha\}_6 \rightarrow \{\alpha\}_5$ cross section.

Exothermic $\{\alpha\}_k \rightarrow \{\alpha\}_l$ transitions are seen to yield larger cross sections than their endothermic $\{\alpha\}_l \rightarrow \{\alpha\}_k$ counterparts. This is because for a given energy with respect to the initial state, radial energy at the avoided crossing is larger in the exothermic case. For the transitions under discussion, this is a favorable condition.

Secondly, as to the behavior of cross-section contributions as a function of the impact parameter, the expected preference of "high-velocity" crossings for high radial velocities translates directly into a preference for small impact parameters (head-on collisions). Likewise, "low-velocity" crossings require grazing or, in any case, glancing collisions at greater impact parameters.

The occurrence of polarization effects in $\{\alpha\}_k \rightarrow \{\alpha\}_l$ cross sections is determined by the relative importance of impact-parameter regions and by the competition between rotational coupling and locking of the electronic angular momentum \mathbf{J} . For head-on collisions ($b \ll R_C$), the orientation of \mathbf{J} remains quite unchanged, irrespective of locking. This holds for both the incoming and outgoing trajectories. Since, for $\text{Ne}^{**}\text{-He}$, avoided crossings are limited to a single Ω value per transition ($\Omega=0^-$ or $\Omega=1$), the preponderance of small impact parameters is equivalent to a large orientation effect. For grazing collisions and large impact parameters ($b \approx R_C$) locking plays no part either (since $R_L \leq R_C$), but the orientation of \mathbf{J} with respect to the internuclear axis undergoes an almost complete "inversion" ($M=0 \rightarrow \Omega=1$, $M=\pm 1 \rightarrow \Omega=0$ for $J=1$). Again, a large but now opposite orientation effect is expected. For intermediate impact parameters and glancing collisions, strong Ω mixing generally leads to an averaging out of orientation effects, unless locking occurs along a substantial part of the trajectory.

Lastly, it is worth noting that rotational coupling inside the crossing radius can play an instrumental role in bringing about a net $\{\alpha\}_k \rightarrow \{\alpha\}_l$ transition in the first place. This happens when the single-transit transition probability approaches unity, as in the $\{\alpha\}_4 \leftrightarrow \{\alpha\}_5$ case.

V. CONCLUDING REMARKS

For the $\text{Ne}^{**}\{\alpha\}_{4,5,6,7}$ group of states, semiclassical considerations are of great help in obtaining insight into the $\text{Ne}^{**} + \text{He}$ intramultiplet-mixing process at thermal energies. Symmetry restraints, Landau-Zener-type radial coupling at avoided crossings, and the competition between rotational coupling and locking, are the essential elements of our simple semiclassical model. The semiclassical calculations, not only qualitatively but more often than not quantitatively as well, effectively emulate quantum-mechanical coupled-channel calculations (which in turn agree well with experiment).

The combination of crossed-beam experiment, quantum-mechanical coupled-channel calculations, and semiclassical analysis presents a picture, of polarization effects in particular, that is quite remarkable in its completeness. The energy dependence of cross sections still needs to be examined in more detail. It will be worthwhile to investigate the possible inclusion of another kind of radial coupling (e.g., Demkov coupling) into the framework of the present model.

In the case of related systems, such as $\text{Ne}^{**}\text{-Ne}$, $\text{Ne}^{**}\text{-H}_2$, or perhaps even $\text{Ne}^{**}\text{-CH}_4$, semiclassical calculations offer a practical way of directly testing the validity of interaction potentials, similar to that for $\text{Ne}^{**}\text{-He}$ but for the changes due to, e.g., a different polarizability. The possible merits of this idea are suggested by preliminary $\text{Ne}^{**}\text{-Ne}$ and $\text{Ne}^{**}\text{-H}_2$ measurements, which show cross-section behavior for these systems to be quite similar to that for $\text{Ne}^{**}\text{-He}$.

¹D. Hennecart and F. Masnou-Seeuws, *J. Phys. B* **18**, 657 (1985).

²(a) W. Buszert, T. Bregel, R. J. Allan, M. W. Ruf, and H. Hotop, *Z. Phys. A* **320**, 105 (1985); (b) W. Buszert, T. Bregel, J. Ganz, K. Harth, A. Siegel, M.-W. Ruf, H. Hotop, and H. Morgner, *J. Phys. (Paris) Colloq.* **46**, C1-199 (1985).

³M. H. Alexander, T. Orlikowski, and J. E. Straub, *Phys. Rev. A* **28**, 73 (1983).

⁴G. Nienhuis, *Phys. Rev. A* **26**, 3137 (1982).

⁵J. G. Kircz, R. Morgenstern, and G. Nienhuis, *Phys. Rev. Lett.* **48**, 610 (1982).

⁶H. A. J. Meyer, H. P. van der Meulen, and R. Morgenstern, *Z. Phys. D* **5**, 299 (1987).

⁷D. Neuschäfer, H. O. Hale, I. V. Hertel, and S. R. Leone, in *Invited Papers of the Fourteenth International Conference on the Physics of Electronic and Atomic Collisions, Palo Alto, 1985*, edited by D. C. Lorents, W. E. Meyerhof, and J. R. Peterson (North-Holland, Amsterdam, 1986).

⁸M. O. Hale, I. V. Hertel, and S. R. Leone, *Phys. Rev. Lett.* **53**, 2296 (1984); M. O. Hale and S. R. Leone, *Phys. Rev. A* **31**,

103 (1985).

⁹J. M. Parson and T. Ishikawa, *J. Chem. Phys.* **80**, 3137 (1984).

¹⁰A. Bähring, I. V. Hertel, E. Meyer, W. Meyer, N. Spies, and H. Schmidt, *J. Phys. B* **17**, 2859 (1984).

¹¹D. Hennecart, *J. Phys. (Paris)* **39**, 1065 (1978); Ph.D. thesis, Université de Caen, Caen, France, 1982.

¹²J. M. Mestdagh, J. Berlande, P. de Pujo, J. Cuvallier, and A. Binet, *Z. Phys. A* **304**, 3 (1982).

¹³E. Düren, E. Hasselbrink, and H. Tischen, *Phys. Rev. Lett.* **50**, 1983 (1983).

¹⁴L. Hüwel, J. Maier, and H. Pauly, *J. Chem. Phys.* **76**, 4961 (1982).

¹⁵H. J. Yuh and P. J. Dagdigian, *Phys. Rev. A* **28**, 63 (1983).

¹⁶N. Böwering, M. R. Bruce, and J. W. Keto, *J. Chem. Phys.* **84**, 709 (1986); **84**, 715 (1986).

¹⁷J. K. Kuh and D. W. Setser, *J. Chem. Phys.* **84**, 4304 (1986).

¹⁸I. V. Hertel, H. Schmidt, A. Bähring, and E. Meyer, *Rep. Prog. Phys.* **48**, 375 (1985).

¹⁹M. P. I. Manders, J. P. J. Driessen, H. C. W. Beijerinck, and B. J. Verhaar, *Phys. Rev. Lett.* **57**, 1577 (1986); **57**, 2472 (1986).

- ²⁰M. P. I. Manders, J. P. J. Driessen, H. C. W. Beijerinck, and B. J. Verhaar, *Phys. Rev. A* **37**, 3237 (1988).
- ²¹M. P. I. Manders, W. M. J. Ruyten, F. v. d. Beucken, J. P. J. Driessen, W. J. T. Veugelers, P. H. Kramer, E. J. D. Vredenburg, W. B. M. van Hoek, G. J. Sandker, H. C. W. Beijerinck, and B. J. Verhaar, *J. Chem. Phys.* **89**, 4777 (1988).
- ²²I. Dabrowski and G. Herzberg, *J. Mol. Spectrosc.* **73**, 183 (1978).
- ²³H. Haberland, W. Konz, and P. Oesterlin, *Phys. B* **15**, 2969 (1982).
- ²⁴J. Raynal, in *Computing as a Language of Physics*, edited by A. E. Salam (IAEA, Vienna, 1972).
- ²⁵R. B. Bernstein, *Atom Molecule Collision Theory* (Plenum, New York, 1979).
- ²⁶A. Messiah, *Quantum Mechanics* (North-Holland, Amsterdam, 1981), Vols. I and II.
- ²⁷L. Landau, *Phys. Z. Sowjetunion* **2**, 46 (1932).
- ²⁸C. Zener, *Proc. R. Soc. London, Ser. A* **137**, 696 (1932).
- ²⁹E. C. G. Stückelberg, *Helv. Phys. Acta* **5**, 369 (1932).
- ³⁰W. R. Thorson, J. B. Delos, and S. A. Boorstein, *Phys. Rev. A* **4**, 1052 (1971).
- ³¹E. E. Nikitin, in *Chemische Elementar Prozesse*, edited by H. Hartmann and J. Heidelberg (Springer-Verlag, Heidelberg, 1968).
- ³²J. B. Delos and W. R. Thorson, *Phys. Rev. A* **6**, 728 (1972).
- ³³E. E. Nikitin, *Adv. Quantum Chem.* **5**, 135 (1970).
- ³⁴V. K. Bykhovskii, E. E. Nikitin, and M. Ya. Orchinnikova, *Zh. Eksp. Teor. Fiz.* **47**, 750 (1964) [*Sov. Phys.—JETP* **20**, 500 (1965)].
- ³⁵J. B. Delos, *Phys. Rev. A* **9**, 1626 (1974).
- ³⁶A. Russek, *Phys. Rev. A* **4**, 1918 (1971).
- ³⁷H. Nakamura and M. Namiki, *Phys. Rev. A* **24**, 2963 (1981).
- ³⁸J. Grosser, *J. Phys. B* **14**, 1449 (1981).
- ³⁹G. Herzberg, *Molecular Spectra and Molecular Structure I: Spectra of Diatomic Molecules* (Van Nostrand, New York, 1950).
- ⁴⁰E. E. Nikitin, *Sov. J. Chem. Phys.* **3**, 1212 (1985).
- ⁴¹C. Gaussorgues and F. Masnou-Seeuws, *J. Phys. B* **10**, 2125 (1977).
- ⁴²Yu. N. Demkov, *Zh. Eksp. Teor. Fiz.* **45**, 195 (1963) [*Sov. Phys.—JETP* **18**, 138 (1964)].